



# CHORUS

This is the accepted manuscript made available via CHORUS. The article has been published as:

## Detecting multimueon jets from the Higgs boson exotic decays in the Higgs portal framework

Jung Chang, Kingman Cheung, Shih-Chieh Hsu, and Chih-Ting Lu

Phys. Rev. D **95**, 035012 — Published 10 February 2017

DOI: [10.1103/PhysRevD.95.035012](https://doi.org/10.1103/PhysRevD.95.035012)

# Detecting multimMuon-jets from the Higgs exotic decays in the Higgs portal framework

Jung Chang<sup>1</sup>, Kingman Cheung<sup>1,2,3</sup>, Shih-Chieh Hsu<sup>3,4</sup>, and Chih-Ting Lu<sup>3</sup>

<sup>1</sup> *Physics Division, National Center for Theoretical Sciences, Hsinchu 300, Taiwan*

<sup>2</sup> *Division of Quantum Phases and Devices, School of Physics,  
Konkuk University, Seoul 143-701, Republic of Korea*

<sup>3</sup> *Department of Physics, National Tsing Hua University, Hsinchu 300, Taiwan*

<sup>4</sup> *Department of Physics, University of Washington at Seattle, Seattle, WA 98195, U.S.A*

A muon-jet ( $\mu$ -jet) is a very special feature that consists of a cluster of collimated muons from the decay of a fast moving light particle of mass about  $\mathcal{O}(1 \text{ GeV})$ . We will use this feature to search for very light particles from rare decays of the Higgs boson. For such a small angular separation of muons which might come from a long-lived particle, both ATLAS and CMS could have the displaced-vertexing-reconstruction capability. We use two simple models of the Higgs-portal type to explore the possibilities of event topologies with two  $2\mu$ -jets, one  $2\mu$ -jet & one  $4\mu$ -jet, and two  $4\mu$ -jets in the final state at LHC-14. We also summarize existing constraints on these models.

## I. INTRODUCTION

A lepton-jet is an object that consists of a group of boosted and collimated leptons. It is a unique signature for the leptonic decay of a fast moving light particle in the mass range below about 1 GeV [1], where it was discussed in the context of light scalar bosons and gauge bosons from the dark sector.

In these dark-sector models, the Higgs boson can be connected the dark sector via Higgs-portal type interaction:  $(\Phi^\dagger\Phi)(S^\dagger S)$ , where  $\Phi$  is the standard model (SM) Higgs field and  $S$  is the scalar field in the dark sector. When both the Higgs field and  $S$  develop vacuum expectation values, the  $\Phi$  and  $S$  mix to form mass eigenstates, and the Higgs boson can decay into a pair of the scalar bosons if kinematically allowed. In some models, the dark sector can also be connected with the SM particles via  $Z - Z'$  mixing. In either scenarios, when the dark scalar bosons or gauge bosons are very light, say below 1 GeV, they will decay into the heaviest SM particles if kinematically allowed. For example, a 500 MeV scalar boson decays, via the mixing with the SM Higgs boson, can decay into a pair of muons, pions, electrons, or photons. The dominant modes would be pions and muons. In some other scenarios when there is a broken  $U(1)$  global symmetry in the dark sector, the scalar boson can also decay into a pair of Goldstone bosons [2]. A UV complete model, which can have one light pseudoscalar resonance ( $a_1$ ) decaying into a pair of muons, is the next-to-minimal supersymmetric standard model (NMSSM) [3]. Both the dark-sector models and the NMSSM have been frequently explored in the LHC experiments: ATLAS [4] and CMS [5].

In this work, we focus on the search for muon-jets from the decay of very light particles so as to identify the existence of dark sectors that are connected to the SM via the Higgs-portal. For simplicity we only consider the dark-sector models that contain either a real SM-singlet scalar field  $X$  or two real SM-singlet scalar fields  $X_1$  and  $X_2$ , without imposing any extra symmetries. The dominant decay modes of the scalar boson of  $\mathcal{O}(1 \text{ GeV})$  would then be pions and muons. It is the muons in the decay products of a fast-moving light scalar boson that form a muon-jet, for which we are searching for in experiments as a signature of the existence of very light scalar bosons. Such a light scalar boson, which originates from the mixing with the SM Higgs boson, can appear in the decay of the Higgs boson. Since the constraints on the mixing for such a light scalar boson with the SM Higgs boson are very strong, which we will show, the very light scalar boson might be a long-lived neutral particle and so we might observe a displaced decay vertex in detectors. We are therefore interested in rare decays of the Higgs boson into a pair of very light scalar bosons of mass about  $\mathcal{O}(1 \text{ GeV})$ , each of which in turns directly decays into a pair of collimated muons or in a cascade decay into another pair of light scalar bosons, then each of them decays into a pair of collimated muons. Let us denote a muon-jet with  $n$  collimated muons in it by  $n\mu$ -jet, e.g., a  $2\mu$ -jet is a muon-jet with 2 muons and a  $4\mu$ -jet is a muon-jet with 4 muons. Thus, the final states can consist of three different types of combinations :

- (1) two  $2\mu$ -jets back-to-back in the transverse plane;
- (2) one  $2\mu$ -jet on one side and one  $4\mu$ -jet on the other side;
- (3) two  $4\mu$ -jets on opposite sides of the transverse plane.

The model can be made further complicated by invoking additional light scalar bosons or gauge bosons in the dark sector such that the decay chain can involve more dark sector particles. At the end, each lepton-jet can consist of more than four leptons, like 6, 8, or more. These lepton-jets would be very interesting objects to search for in experiments because they are clear signals of new physics. The experimental resolution to tell the number of leptons in a lepton-jet becomes an important issue. Here we only consider two simple cases of two muons inside a muon-jet and four muons inside a “fat” muon-jet. We also compare these two cases to distinguish between whether the final state muon-jet is produced from direct decay of a light scalar boson or in a cascade decay.

The main goal of this work is to investigate the capability of the LHC detectors (especially the ATLAS because of its size) of observing muon-jets in search of rare decays of the Higgs bosons into a pair of very light bosons, which may decay directly into muon-jets or indirectly via subsequent decays into other lighter bosons. We found that if the light Higgs boson heavier than about 0.3 GeV, the ATLAS detector has a good chance of seeing that.

We would like to remind the readers that the model considered in this work is only a toy-model of the Higgs-portal type models. The other popular models such as dark- $Z$  and dark-photon fall in the same category of models in the present context. Nevertheless, the search for dark-photon or dark- $Z$  also includes the electron-jets and pion-jets. The choice depends on the branching ratios and also the capability of the detector. In the present work, we simply focus on the best capability of observing muon-jets using the tracker and muon spectrometer at the ATLAS or CMS detector.

The organization is as follows. We describe two simple Higgs-portal models in the next section, and in Sec. III the existing constraints on these two models. These constraints are quite generic on many models of this kind. We consider some kinematical distributions at the LHC for some benchmark points in Sec. IV and highlight the potential search at LHC-14 with  $300 \text{ fb}^{-1}$  in Sec. V. Finally, we conclude in Sec. VI.

## II. HIGGS-PORTAL MODELS

### A. Higgs-portal Model-1 : Only one light scalar $h_s$

Here we employ a Higgs portal model in which the SM Higgs field  $\Phi$  can mix with a real scalar field  $X$ . This additional scalar field does not have any SM interactions. We also impose a  $Z_2$  symmetry which  $\Phi$  is  $Z_2$  – *even* and  $X$  is  $Z_2$  – *odd* before both the Higgs field and  $X$  develop vacuum expectation values. The renormalizable Lagrangian density for this model is given by

$$\mathcal{L} = \frac{1}{2}\partial_\mu X \partial^\mu X + \frac{1}{2}\mu_X^2 X^2 - \frac{1}{4}\lambda_X X^4 - \frac{1}{2}\lambda_{\Phi X}(\Phi^\dagger \Phi)X^2 + \mathcal{L}_{SM}, \quad (1)$$

where the Higgs sector in the  $\mathcal{L}_{SM}$  is

$$\mathcal{L}_{SM} \supset (D_\mu \Phi)^\dagger (D^\mu \Phi) + \mu^2(\Phi^\dagger \Phi) - \lambda(\Phi^\dagger \Phi)^2. \quad (2)$$

After the electroweak symmetry breaking (EWSB), the SM Higgs doublet field  $\Phi$  is expanded around its vacuum-expectation value:

$$\Phi(x) = \frac{1}{\sqrt{2}} \begin{pmatrix} 0 \\ \langle \phi \rangle + \phi(x) \end{pmatrix} \quad (3)$$

where  $\langle \phi \rangle \approx 246$  GeV. The  $X$  is also expanded around its vacuum-expectation value  $\langle \chi \rangle$ :

$$X(x) = \langle \chi \rangle + \chi(x) \quad (4)$$

Two tadpole conditions can be written down using  $\partial V/\partial \phi = 0$  and  $\partial V/\partial \chi = 0$ , where  $V$  is the scalar potential part of Eq. (1):

$$\langle \phi \rangle^2 = \frac{4\lambda_X \mu^2 - 2\lambda_{\Phi X} \mu_X^2}{4\lambda\lambda_X - \lambda_{\Phi X}^2}, \quad (5)$$

$$\langle \chi \rangle^2 = \frac{4\lambda\mu_X^2 - 2\lambda_{\Phi X}\mu^2}{4\lambda\lambda_X - \lambda_{\Phi X}^2} \quad (6)$$

Taking the decoupling limit  $\lambda_{\Phi X} \rightarrow 0$  from the above equations, we recover the SM condition of  $\langle \phi \rangle^2 = \mu^2/\lambda$  as well as  $\langle \chi \rangle^2 = \mu_X^2/\lambda_X$ .

It is easy to see that the Higgs boson field  $\phi$  will mix with the new scalar field  $\chi$  to form mass eigenstates denoted by  $h$  and  $h_s$ , respectively. The mass terms for the Higgs boson and the new scalar boson are

$$\mathcal{L}_m = -\frac{1}{2} (\phi \ \chi) \begin{pmatrix} 2\lambda\langle \phi \rangle^2 & \lambda_{\Phi X}\langle \phi \rangle\langle \chi \rangle \\ \lambda_{\Phi X}\langle \phi \rangle\langle \chi \rangle & 2\lambda_X\langle \chi \rangle^2 \end{pmatrix} \begin{pmatrix} \phi \\ \chi \end{pmatrix}, \quad (7)$$

We can rotate  $(\phi \ \chi)^T \rightarrow (h \ h_s)^T$  through an angle  $\theta$

$$\begin{pmatrix} h \\ h_s \end{pmatrix} = \begin{pmatrix} \cos \theta & \sin \theta \\ -\sin \theta & \cos \theta \end{pmatrix} \begin{pmatrix} \phi \\ \chi \end{pmatrix} \quad (8)$$

Thus, the masses of the Higgs boson  $h$  and the scalar boson  $h_s$ , the mixing angle  $\theta$ , and the interaction governing  $h \rightarrow h_s h_s$  are given by, in terms of the parameters in Eq. (1),

$$\begin{aligned} m_h^2 &= 2\lambda\langle \phi \rangle^2 \cos^2 \theta + 2\lambda_X\langle \chi \rangle^2 \sin^2 \theta + \lambda_{\Phi X}\langle \phi \rangle\langle \chi \rangle \sin 2\theta \\ m_{h_s}^2 &= 2\lambda_X\langle \chi \rangle^2 \cos^2 \theta + 2\lambda\langle \phi \rangle^2 \sin^2 \theta - \lambda_{\Phi X}\langle \phi \rangle\langle \chi \rangle \sin 2\theta \\ \mathcal{L}_{hh_s h_s} &= -\frac{1}{2}[6\lambda_X\langle \chi \rangle \cos^2 \theta \sin \theta + 6\lambda\langle \phi \rangle \cos \theta \sin^2 \theta + \lambda_{\Phi X}\langle \phi \rangle(\cos^3 \theta - 2\cos \theta \sin^2 \theta) \\ &\quad + \lambda_{\Phi X}\langle \chi \rangle(\sin^3 \theta - 2\cos^2 \theta \sin \theta)]hh_s h_s \\ \tan 2\theta &= \frac{\lambda_{\Phi X}\langle \phi \rangle\langle \chi \rangle}{\lambda\langle \phi \rangle^2 - \lambda_X\langle \chi \rangle^2} \end{aligned}$$

In the next section, where we describe the constraints on the model, the angle  $\theta$  has to be very small. In the small  $\theta$  limit, the above relations are reduced to

$$\begin{aligned} m_h^2 &\simeq 2\lambda\langle\phi\rangle^2 = (125 \text{ GeV})^2 \\ m_{h_s}^2 &\simeq 2\lambda_X\langle\chi\rangle^2 \\ \mathcal{L}_{hh_s h_s} &= -\frac{1}{2}\lambda_{\Phi X}\langle\phi\rangle hh_s h_s \\ \theta &\simeq \frac{\lambda_{\Phi X}\langle\phi\rangle\langle\chi\rangle}{m_h^2 - m_{h_s}^2}, \end{aligned}$$

The scalar boson  $h_s$  can decay into SM particles via the mixing with the Higgs boson. Thus, the decay widths for  $h_s \rightarrow \ell^+\ell^-$  and  $h_s \rightarrow \pi\pi$  are given by [6]

$$\Gamma(h_s \rightarrow \ell^+\ell^-) = \sin^2\theta \frac{m_\ell^2 m_{h_s}}{8\pi\langle\phi\rangle^2} \left(1 - \frac{4m_\ell^2}{m_{h_s}^2}\right)^{3/2}, \quad (9)$$

$$\Gamma(h_s \rightarrow \pi\pi) = \sin^2\theta \frac{m_{h_s}^3}{216\pi\langle\phi\rangle^2} \left(1 - \frac{4m_\pi^2}{m_{h_s}^2}\right)^{1/2} \left(1 + \frac{11m_\pi^2}{2m_{h_s}^2}\right)^2, \quad (10)$$

$$\Gamma_{h_s} = \frac{1}{\tau_{h_s}} = \sum_{\ell=e,\mu} \Gamma(h_s \rightarrow \ell^+\ell^-) + \sum_{\pi\pi=\pi^+\pi^-, \pi^0\pi^0} \Gamma(h_s \rightarrow \pi\pi), \quad (11)$$

where we have restricted  $m_{h_s} \lesssim 1$  GeV. <sup>1</sup> Here  $\pi\pi$  includes both  $\pi^+\pi^-$  and  $\pi^0\pi^0$ , and  $\Gamma(h_s \rightarrow \pi^+\pi^-) = 2\Gamma(h_s \rightarrow \pi^0\pi^0)$ . Since the tree-level estimate of  $\Gamma(h_s \rightarrow \pi\pi)$  is not adequate when  $m_{h_s}$  is not far from the pion threshold, where the strong final-state interaction becomes important [8, 9], so we follow Ref. [8, 9] for numerical estimates of  $\Gamma(h_s \rightarrow \pi\pi)$ . We show the branching ratios of the scalar boson  $h_s$  for the two most dominant modes  $\mu^+\mu^-$  and  $\pi\pi$  in Table I for  $m_{h_s} = 0.3 - 1$  GeV.

TABLE I. The branching ratio for the most two dominant decay modes of the scalar boson  $h_s$  for  $m_{h_s} = 0.3 - 1$  GeV. Here  $\pi\pi$  includes  $\pi^+\pi^-$  and  $\pi^0\pi^0$ .

$m_{h_s}$ (GeV)	0.3	0.4	0.5	0.6	0.7	0.8	0.9	1.0
$B(\mu^+\mu^-)$	40%	12.5%	10%	8%	6%	4.5%	1.5%	0.4%
$B(\pi\pi)$	60%	87.5%	90%	92%	94%	95.5%	98.5%	99.6%

### B. Higgs-portal model-2 : Two light scalars : $h_{D_1}, h_{D_2}$

We can extend our Higgs-portal model-1 to include two real scalar fields  $X_1$  and  $X_2$ , which can mix with the SM Higgs field but do not have any SM interactions. We also impose a  $Z_2$  symmetry which  $\Phi$  is  $Z_2 - \text{even}$  and both  $X_1, X_2$  are  $Z_2 - \text{odd}$  before these Higgs field,  $X_1$  and  $X_2$  develop vacuum expectation values. The renormalizable Lagrangian density for this model is given by

$$\begin{aligned} \mathcal{L} &= \frac{1}{2}\partial_\mu X_1 \partial^\mu X_1 + \frac{1}{2}\mu_1^2 X_1^2 \\ &+ \frac{1}{2}\partial_\mu X_2 \partial^\mu X_2 + \frac{1}{2}\mu_2^2 X_2^2 \\ &- \lambda_{\Phi X}(\Phi^\dagger\Phi)(X_1 + \alpha X_2)^2 - \lambda_{X_1 X_2}(X_1 + \beta X_2)^4 \\ &+ \mathcal{L}_{SM}, \end{aligned} \quad (12)$$

where the Higgs sector in the  $\mathcal{L}_{SM}$  is

$$\mathcal{L}_{SM} \supset (D_\mu\Phi)^\dagger(D^\mu\Phi) + \mu^2(\Phi^\dagger\Phi) - \lambda(\Phi^\dagger\Phi)^2. \quad (13)$$

<sup>1</sup> Even though the major decay mode of  $m_{h_s} = 0.3 - 1$  GeV is  $\pi\pi$  mode, we still focus on the analysis of  $\mu^+\mu^-$  mode. Since the resolution of muons are better than pions and the analysis of  $\pi\pi$  mode has been researched in Ref.[2, 7].

After the electroweak symmetry breaking (EWSB), the SM Higgs doublet field  $\Phi$  is expanded around its vacuum-expectation value:

$$\Phi(x) = \frac{1}{\sqrt{2}} \begin{pmatrix} 0 \\ \langle \phi \rangle + \phi(x) \end{pmatrix} \quad (14)$$

where  $\langle \phi \rangle \approx 246$  GeV. Both  $X_1$  and  $X_2$  are also expanded around their vacuum-expectation values  $\langle \chi_{1/2} \rangle$ :

$$X_{1/2}(x) = \langle \chi_{1/2} \rangle + \chi_{1/2}(x) \quad (15)$$

Three tadpole conditions can be written down using  $\partial V / \partial \phi = 0$ ,  $\partial V / \partial \chi_1 = 0$ , and  $\partial V / \partial \chi_2 = 0$ , where  $V$  is the scalar potential part of Eq. (12):

$$\langle \phi \rangle^2 = \frac{\mu^2 - \lambda_{\Phi X} (\langle \chi_1 \rangle + \alpha \langle \chi_2 \rangle)^2}{\lambda}, \quad (16)$$

$$\langle \chi_1 \rangle^2 = \frac{\mu_1^2 \mu_2^2 - \lambda_{\Phi X} (\alpha^2 \mu_1^2 - \mu_2^2) \langle \phi \rangle^2}{\lambda_{X_1 X_2} (\mu_2^2 + \beta \mu_1^2 - (\alpha - \beta)^2 \lambda_{\Phi X} \langle \phi \rangle^2)^3} \cdot (\mu_2^2 - \lambda_{\Phi X} \alpha (\alpha - \beta) \langle \phi \rangle^2)^2, \quad (17)$$

$$\langle \chi_2 \rangle^2 = \frac{\mu_1^2 \mu_2^2 - \lambda_{\Phi X} (\alpha^2 \mu_1^2 - \mu_2^2) \langle \phi \rangle^2}{\lambda_{X_1 X_2} (\mu_2^2 + \beta \mu_1^2 - (\alpha - \beta)^2 \lambda_{\Phi X} \langle \phi \rangle^2)^3} \cdot (\beta \mu_1^2 + \lambda_{\Phi X} (\alpha - \beta) \langle \phi \rangle^2)^2 \quad (18)$$

Taking the decoupling limit  $\lambda_{\Phi X} \rightarrow 0$  from the above equations, we recover the SM condition of  $\langle \phi \rangle^2 = \mu^2 / \lambda$  as well as  $\langle \chi_1 \rangle^2 = \frac{\mu_1^2}{\lambda_{X_1 X_2} [1 + \beta (\frac{\mu_1}{\mu_2})^2]^3}$  and  $\langle \chi_2 \rangle^2 = \frac{\beta^2 \mu_2^2}{\lambda_{X_1 X_2} [\beta + (\frac{\mu_2}{\mu_1})^2]^3}$ .

It is easy to see that the Higgs boson  $\phi$  will mix with these two new scalar bosons  $\chi_1$  and  $\chi_2$  to form mass eigenstates denoted by  $h$ ,  $h_{D_1}$  and  $h_{D_2}$ , respectively. The mass terms for the Higgs boson and these two new scalar bosons are

$$\mathcal{L}_m = -\frac{1}{2} (\phi \ \chi_1 \ \chi_2) \begin{pmatrix} 2\lambda \langle \phi \rangle^2 & 2\lambda_{\Phi X} \langle \phi \rangle \langle \chi_\alpha \rangle & 2\lambda_{\Phi X} \alpha \langle \phi \rangle \langle \chi_\alpha \rangle \\ 2\lambda_{\Phi X} \langle \phi \rangle \langle \chi_\alpha \rangle & -\mu_1^2 + 12\lambda_{X_1 X_2} \langle \chi_\beta \rangle^2 & 12\lambda_{X_1 X_2} \beta \langle \chi_\beta \rangle^2 \\ 2\lambda_{\Phi X} \alpha \langle \phi \rangle \langle \chi_\alpha \rangle & 12\lambda_{X_1 X_2} \beta \langle \chi_\beta \rangle^2 & -\mu_2^2 + 12\lambda_{X_1 X_2} \beta^2 \langle \chi_\beta \rangle^2 \end{pmatrix} \begin{pmatrix} \phi \\ \chi_1 \\ \chi_2 \end{pmatrix}, \quad (19)$$

where we set  $\langle \chi_1 \rangle + \alpha \langle \chi_2 \rangle \equiv \langle \chi_\alpha \rangle$  and  $\langle \chi_1 \rangle + \beta \langle \chi_2 \rangle \equiv \langle \chi_\beta \rangle$ . We can rotate  $(\phi \ \chi_1 \ \chi_2)^T \rightarrow (h \ h_{D_1} \ h_{D_2})^T$  through these angles  $\theta_1$ ,  $\theta_2$  and  $\theta_3$

$$\begin{pmatrix} h \\ h_{D_1} \\ h_{D_2} \end{pmatrix} = \begin{pmatrix} \cos \theta_1 & \sin \theta_1 & 0 \\ -\sin \theta_1 & \cos \theta_1 & 0 \\ 0 & 0 & 1 \end{pmatrix} \begin{pmatrix} \cos \theta_2 & 0 & \sin \theta_2 \\ 0 & 1 & 0 \\ -\sin \theta_2 & 0 & \cos \theta_2 \end{pmatrix} \begin{pmatrix} 1 & 0 & 0 \\ 0 & \cos \theta_3 & \sin \theta_3 \\ 0 & -\sin \theta_3 & \cos \theta_3 \end{pmatrix} \begin{pmatrix} \phi \\ \chi_1 \\ \chi_2 \end{pmatrix} \quad (20)$$

$$= \begin{pmatrix} C_{\theta_1} C_{\theta_2} & (S_{\theta_1} C_{\theta_3} - C_{\theta_1} S_{\theta_2} S_{\theta_3}) & (S_{\theta_1} S_{\theta_3} + C_{\theta_1} S_{\theta_2} C_{\theta_3}) \\ -S_{\theta_1} C_{\theta_2} & (C_{\theta_1} C_{\theta_3} + S_{\theta_1} S_{\theta_2} S_{\theta_3}) & (C_{\theta_1} S_{\theta_3} - S_{\theta_1} S_{\theta_2} C_{\theta_3}) \\ -S_{\theta_2} & -C_{\theta_2} S_{\theta_3} & C_{\theta_2} C_{\theta_3} \end{pmatrix} \begin{pmatrix} \phi \\ \chi_1 \\ \chi_2 \end{pmatrix} \quad (21)$$

where  $\theta_{1,2,3}$  is the mixing angle between  $\phi$  and  $\chi_1$ , between  $\phi$  and  $\chi_2$ , and between  $\chi_1$  and  $\chi_2$ , respectively.  $C_{\theta_i}$  stands for  $\cos \theta_i$  and  $S_{\theta_i}$  stands for  $\sin \theta_i$ . If we assume both  $\chi_1$  and  $\chi_2$  mixings with  $\phi$  are very small ( $\theta_1, \theta_2$  are very small), then it implies that  $\lambda_{\Phi X}$  is small compared to other parameters. Thus, the masses of the Higgs boson  $h$  and two scalar bosons  $h_{D_1}$ ,  $h_{D_2}$ , and the interaction governing  $h \rightarrow h_{D_1} h_{D_1}$ ,  $h \rightarrow h_{D_2} h_{D_2}$ ,  $h \rightarrow h_{D_1} h_{D_2}$ , and  $h_{D_1} \rightarrow h_{D_2} h_{D_2}$  are given by, in terms of the parameters in Eq. (12) in the small  $\theta_1, \theta_2$  limit,

$$\begin{aligned} m_h^2 &\simeq 2\lambda \langle \phi \rangle^2 - [(\mu_1^2 - 12\lambda_{X_1 X_2} \langle \chi_\beta \rangle^2) \sin^2 \theta_1 + (\mu_2^2 - 12\lambda_{X_1 X_2} \beta^2 \langle \chi_\beta \rangle^2) \sin^2 \theta_2] \\ &\quad + 2\lambda_{\Phi X} \langle \phi \rangle \langle \chi_\alpha \rangle (\sin 2\theta_1 + \alpha \sin 2\theta_2) \\ &= (125 \text{ GeV})^2 \\ m_{h_{D_1}}^2 &\simeq (-\mu_1^2 + 12\lambda_{X_1 X_2} \langle \chi_\beta \rangle^2) \cos^2 \theta_3 + (-\mu_2^2 + 12\lambda_{X_1 X_2} \beta^2 \langle \chi_\beta \rangle^2) \sin^2 \theta_3 \\ &\quad + 12\lambda_{X_1 X_2} \beta \langle \chi_\beta \rangle^2 \sin 2\theta_3 \\ &\quad + 2\lambda \langle \phi \rangle^2 \sin^2 \theta_1 - 2\lambda_{\Phi X} \langle \phi \rangle \langle \chi_\alpha \rangle \sin 2\theta_1 \\ m_{h_{D_2}}^2 &\simeq (-\mu_1^2 + 12\lambda_{X_1 X_2} \langle \chi_\beta \rangle^2) \sin^2 \theta_3 + (-\mu_2^2 + 12\lambda_{X_1 X_2} \beta^2 \langle \chi_\beta \rangle^2) \cos^2 \theta_3 \\ &\quad - 12\lambda_{X_1 X_2} \beta \langle \chi_\beta \rangle^2 \sin 2\theta_3 \\ &\quad + 2\lambda \langle \phi \rangle^2 \sin^2 \theta_2 - 2\lambda_{\Phi X} \alpha \langle \phi \rangle \langle \chi_\alpha \rangle \sin 2\theta_2 \end{aligned}$$

$$\mathcal{L}_{hh_{D_1}h_{D_1}} \simeq -\lambda_{\Phi X}\langle\phi\rangle hh_{D_1}h_{D_1} \quad (22)$$

$$\mathcal{L}_{hh_{D_2}h_{D_2}} \simeq -\lambda_{\Phi X}\alpha^2\langle\phi\rangle hh_{D_2}h_{D_2} \quad (23)$$

$$\mathcal{L}_{hh_{D_1}h_{D_2}} \simeq -2\lambda_{\Phi X}\alpha\langle\phi\rangle hh_{D_1}h_{D_2} \quad (24)$$

$$\begin{aligned} \mathcal{L}_{h_{D_1}h_{D_2}h_{D_2}} &\simeq -\frac{1}{2}[24\lambda_{X_1X_2}\langle\chi\beta\rangle(\beta^2\cos^3\theta_3 + \beta(\beta^2 - 2)\cos^2\theta_3\sin\theta_3 \\ &\quad + (1 - 2\beta^2)\cos\theta_3\sin^2\theta_3 + \beta\sin^3\theta_3)]h_{D_1}h_{D_2}h_{D_2} \\ &\equiv \frac{\mu_{HD}}{2}h_{D_1}h_{D_2}h_{D_2} \end{aligned} \quad (25)$$

Here we assume  $m_{h_{D_1}} > 2m_{h_{D_2}}$  and  $h_{D_1}$  decays dominantly into  $h_{D_2}h_{D_2}$ , i.e.  $B(h_{D_1} \rightarrow h_{D_2}h_{D_2}) > 99\%$ , then we can use this property to pin down the decay width of  $h_{D_1}$  as

$$\Gamma_{h_{D_1}} = \frac{1}{\tau_{h_{D_1}}} \approx \frac{\mu_{HD}^2}{32\pi m_{h_{D_1}}} \times \sqrt{1 - 4\left(\frac{m_{h_{D_2}}}{m_{h_{D_1}}}\right)^2}. \quad (26)$$

The properties of the other scalar boson  $h_{D_2}$  are the same as the scalar boson  $h_s$  in Higgs portal model-1. Thus, the partial widths for  $h_{D_2} \rightarrow \ell^+\ell^-$  and  $h_{D_2} \rightarrow \pi\pi$  are given by [6]

$$\Gamma(h_{D_2} \rightarrow \ell^+\ell^-) = \sin^2\theta_2 \frac{m_\ell^2 m_{h_{D_2}}}{8\pi\langle\phi\rangle^2} \left(1 - \frac{4m_\ell^2}{m_{h_{D_2}}^2}\right)^{3/2}, \quad (27)$$

$$\Gamma(h_{D_2} \rightarrow \pi\pi) = \sin^2\theta_2 \frac{m_{h_{D_2}}^3}{216\pi\langle\phi\rangle^2} \left(1 - \frac{4m_\pi^2}{m_{h_{D_2}}^2}\right)^{1/2} \left(1 + \frac{11m_\pi^2}{2m_{h_{D_2}}^2}\right)^2, \quad (28)$$

$$\Gamma_{h_{D_2}} = \frac{1}{\tau_{h_{D_2}}} = \sum_{\ell=e,\mu} \Gamma(h_{D_2} \rightarrow \ell^+\ell^-) + \sum_{\pi=\pi^+,\pi^0} \Gamma(h_{D_2} \rightarrow \pi\pi), \quad (29)$$

where we have also restricted  $m_{h_{D_2}} \lesssim 1$  GeV.

### III. CONSTRAINTS

There are a number of existing constraints on these two Higgs-portal models. All these constraints are quite generic for any light scalar boson, which is originally a SM singlet but mixes with the Higgs boson and thus can decay into SM fermions and the Higgs boson can decay into a pair of such scalar bosons.

The first constraint comes from a global fit to the Higgs signal strengths and it constrains the nonstandard decay of the Higgs boson to be less than 0.94 MeV using the most current data in Summer 2014 [10]. The partial width for  $h \rightarrow h_s h_s$  is

$$\Gamma(h \rightarrow h_s h_s) \simeq \frac{\langle\phi\rangle^2}{32\pi m_h} (\lambda_{\Phi X})^2 < 0.94 \text{ MeV}. \quad (30)$$

It gives a relation

$$|\lambda_{\Phi X}| < 0.014. \quad (31)$$

For the Higgs-portal model-2, we can use the same method to constrain various partial widths of  $h \rightarrow h_{D_1}h_{D_1}$ ,  $h \rightarrow h_{D_2}h_{D_2}$  and  $h \rightarrow h_{D_1}h_{D_2}$  as follows.

$$\Gamma(h \rightarrow h_{D_1}h_{D_1}) \simeq \frac{\langle\phi\rangle^2}{32\pi m_h} (2\lambda_{\Phi X})^2 \quad (32)$$

$$\Gamma(h \rightarrow h_{D_2}h_{D_2}) \simeq \frac{\langle\phi\rangle^2}{32\pi m_h} (2\lambda_{\Phi X}\alpha^2)^2 \quad (33)$$

$$\Gamma(h \rightarrow h_{D_1}h_{D_2}) \simeq \frac{\langle\phi\rangle^2}{16\pi m_h} (2\lambda_{\Phi X}\alpha)^2 \quad (34)$$

$$\begin{aligned}
& \Gamma(h \rightarrow h_{D_1} h_{D_1}) + \Gamma(h \rightarrow h_{D_2} h_{D_2}) + \Gamma(h \rightarrow h_{D_1} h_{D_2}) \\
& \simeq \frac{\langle \phi \rangle^2}{32\pi m_h} (2\lambda_{\Phi X})^2 (1 + \alpha^4 + 2\alpha^2) < 0.94 \text{ MeV} \\
& \Rightarrow |\lambda_{\Phi X}(1 + \alpha^2)| < 6.99 \times 10^{-3}.
\end{aligned} \tag{35}$$

Another set of constraints come from the decays of  $B$  mesons [12, 13] summarized in Ref. [11].

- For  $100 \text{ MeV} < m_{h_s} < 210 \text{ MeV}$  the scalar boson  $h_s$  can only decay into a pair of electron and positron but the decay length is so long that it leaves no track or energy within the detector. The search for  $B \rightarrow K + \text{invisible}$  and fixed target experiments constrain  $\sin^2 \theta \lesssim 10^{-8}$ .
- For  $210 \text{ MeV} < m_{h_s} < 280 \text{ MeV}$  the scalar boson  $h_s$  can decay into a pair of muons, fixed target experiments and the search for  $B \rightarrow K \mu^+ \mu^-$  in LHCb and B factories constrain  $\sin^2 \theta \lesssim 10^{-10}$ .
- For  $280 \text{ MeV} < m_{h_s} < 360 \text{ MeV}$  the same experiments constrain  $\sin^2 \theta \lesssim 10^{-10}$ , except for a window between  $10^{-8} \lesssim \sin^2 \theta \lesssim 10^{-5}$ .
- For  $360 \text{ MeV} < m_{h_s} < 4.8 \text{ GeV}$  the experimental search for  $B \rightarrow K \mu^+ \mu^-$  in LHCb and B factories constrain  $\sin^2 \theta \times B(h_s \rightarrow \mu^+ \mu^-) \lesssim 10^{-6}$ .

For the constraint of  $B \rightarrow K \mu^+ \mu^-$ , we follow Ref. [11] and use the formula

$$Br(B \rightarrow K h_s) \times Br(h_s \rightarrow \mu^+ \mu^-) \times \int_0^\pi \frac{\sin \theta d\theta}{2} (1 - \exp[\frac{-l_{xy}}{\sin \theta} \frac{1}{\gamma \beta c \tau}]) \tag{36}$$

where  $l_{xy}$  is the maximum reconstructed transverse decay distance from the beampipe,  $\gamma$ ,  $\beta c$  and  $\tau$  are the boost factor, speed, and lifetime of  $h_s$ .<sup>2</sup>

We summarize all these constraints in Fig. 1. Here we also plot beyond the limit of the displaced muon reconstruction for decay length  $\sim 6m$  in the ATLAS (the orange region) and  $\sim 4m$  in the CMS (the yellow region) for our analysis below.

Since the properties of the scalar boson  $h_{D_2}$  in Higgs-portal model-2 are the same as the scalar boson  $h_s$  in Higgs-portal model-1, we can also apply the constraints in Fig.1 to  $m_{h_{D_2}}$ .

The third constraint, which is specific to the two  $2\mu$ -jets case, comes from the recent search of  $h \rightarrow 2a \rightarrow 2(\mu^+ \mu^-) + X$  by the CMS at the 8 TeV LHC [15], where  $a$  is a light scalar or pseudoscalar in the mass range of  $2m_\mu < m_a < 2m_\tau$ . The search limits at the 95% CL is

$$\sigma(pp \rightarrow 2a + X) B^2(a \rightarrow 2\mu) \times \epsilon_{data} \times \mathcal{L} \leq N(m_{\mu\mu}) = 3.1 + 1.2 \exp(-\frac{(m_{\mu\mu} - 0.32)^2}{2 \times 0.03^2}), \tag{37}$$

where  $\epsilon_{data}$  is the experimental data efficiency,  $m_{\mu\mu}$  is the dimuon mass and  $\mathcal{L} = 20.7 \text{ fb}^{-1}$ .<sup>3</sup> We follow closely the analysis performed in Ref. [15] at the 8 TeV run with  $\sigma(pp \rightarrow h) = 19 \text{ pb}$  [19]. The branching ratio for  $B(h_s \rightarrow \mu^+ \mu^-)$  is shown in Table I, and the branching ratio  $B(h \rightarrow h_s h_s)$  is given by  $\frac{\Gamma(h \rightarrow h_s h_s)}{\Gamma_h + \Gamma(h \rightarrow h_s h_s)}$ , where  $\Gamma_h \simeq 4.0 \text{ MeV}$ . The details of detector efficiencies will be shown in Sec. V. However, the new light boson is restricted to decay with transverse decay length  $L_{xy} < 4.4 \text{ cm}$  and longitudinal decay length  $L_z < 34.5 \text{ cm}$  in Ref. [15], which are not suitable for  $m_{h_s} \sim 0.3 \text{ GeV}$  in our Higgs-portal model. Finally, we found this constraint is only applicable for  $m_{h_s} = 0.4 - 0.8 \text{ GeV}$  and gives the constraint  $|\lambda_{\Phi X}| < 0.007 - 0.026$  in the Higgs-portal model-1. To be conservative, we choose  $|\lambda_{\Phi X}| = 0.007$  for  $m_{h_s} = 0.4 - 1.0 \text{ GeV}$  in the following analysis.

Similarly, this constraint is also only applicable for  $m_{h_{D_2}} = 0.4 - 0.8 \text{ GeV}$  and gives the constraint  $2|\lambda_{\Phi X}| \alpha^2 < 0.007 - 0.026$  in the Higgs-portal model-2.

#### IV. KINEMATICAL DISTRIBUTIONS FOR THESE HIGGS PORTAL MODELS WITH BENCHMARK POINTS

A lepton-jet is a very special and unique object at colliders. In the Higgs-portal models considered in this work, the light scalars can decay into leptons and pions. We focus on the 2 or 4 muons modes in this work. Taking into

<sup>2</sup> Since B mesons are produced with a higher boost at LHCb than B factories, the integral factor  $\int_0^\pi \frac{\sin \theta d\theta}{2} (1 - \exp[\frac{-l_{xy}}{\sin \theta} \frac{1}{\gamma \beta c \tau}])$  for the case of LHCb will be smaller than B factories as pointed out in Ref [14]. Here we simply assume these two integral factors are similar, and the results are consistent with Ref [14] within uncertainties.

<sup>3</sup> There are a few other similar searches [15] at the LHC, but the mass ranges are outside 1 GeV and not relevant to the current work.

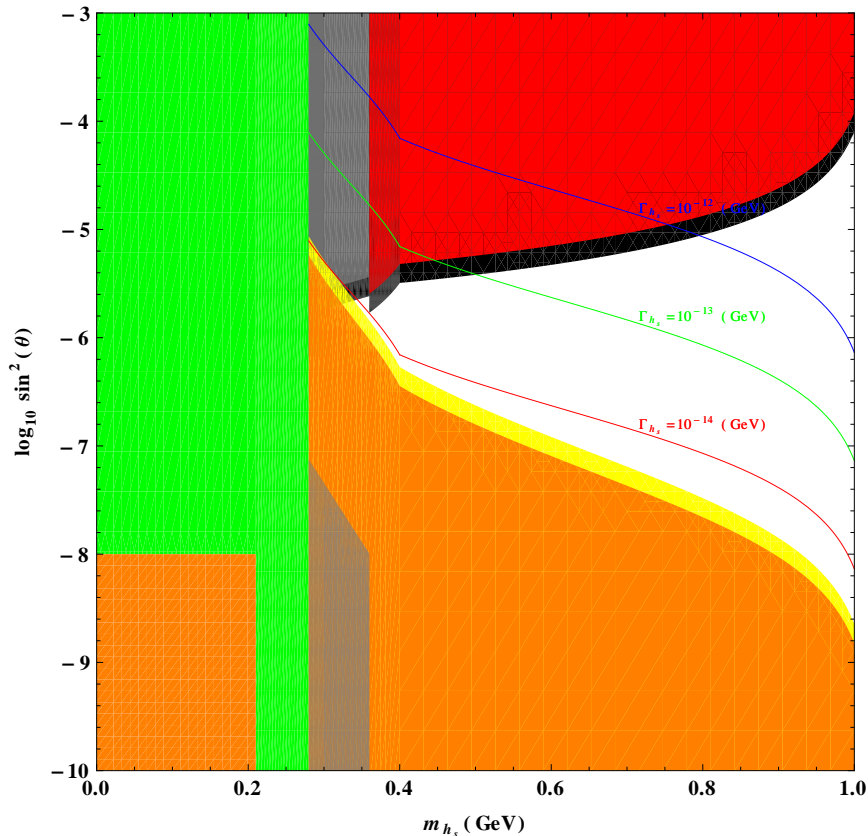


FIG. 1. Existing constraints on the Higgs-portal model-1 in the plane of  $\log_{10} \sin^2 \theta$  vs  $m_{h_s}$ . The green region is for  $m_{h_s} < 280$  MeV which is ruled out by fixed target experiments,  $B \rightarrow K + \text{invisible}$  and  $B \rightarrow K\mu^+\mu^-$ . The gray one for  $280 \text{ MeV} < m_{h_s} < 360$  MeV, and the red one for  $360 \text{ MeV} < m_{h_s} < 1$  GeV, which are ruled out by fixed target experiments and  $B \rightarrow K\mu^+\mu^-$  in B factories. The black region for  $280 \text{ MeV} < m_{h_s} < 1$  GeV which is ruled out by  $B \rightarrow K\mu^+\mu^-$  in LHCb [12, 13]. The orange and yellow regions show beyond the limit of displaced muon reconstruction for the ATLAS and CMS detector, respectively. The white region then stands for the allowed parameter space and possible muon reconstruction inside detectors. The solid lines are contours of various decay widths of  $h_s$ .

account the constraints that we have presented in the previous section, we explore the signatures for a few possible benchmark points for the Higgs-portal model-1 and -2, and also show the characteristics of  $2\mu$ -jets or  $4\mu$ -jets in the final state.

While we collect most of the kinematic distributions in appendix, here we only illustrate the distributions which are the most relevant to the muon-jets, namely, the angular separation among the muons within a muon-jet.

### A. Higgs-portal model-1

In the Higgs-portal model-1, there is only one light scalar boson in the dark sector. The dominant muon-jet process comes from gluon fusion into the Higgs boson, followed by the Higgs decay into a pair of light scalar bosons,  $h \rightarrow h_s h_s$ . Finally, each  $h_s$  decays into a pair of opposite-sign muons. The Feynman diagram for this process is shown in Fig. 2.

The final state of this signal process consists of four muons, which are organized into two dimuon pairs. Each dimuon pair consists of two extremely collimated oppositely-charged muons. The angular separation is of order  $O(0.01)$ . These two dimuon pairs are back-to-back in the transverse plane. We focus on  $m_{h_s} = 0.4 - 1.0$  GeV for varying  $\sin \theta$  as the benchmark points in Table II. Here we also include the estimates of the lab-frame decay length ( $\gamma c\tau$ ) for  $h_s$ , where  $\gamma c\tau \approx \frac{2}{\Delta R} \times c\tau$  and  $\Delta R \approx 2m_{h_s}/P_{T_{h_s}}$ . While we display most distributions in appendix, here we show the distribution for the opening angle  $\Delta R_{\mu^+\mu^-}$  for a pair oppositely-charged muons inside a muon-jet in Fig. 3 for each benchmark point.

The cross section for two  $2\mu$ -jets in Higgs-portal model-1 is

$$\sigma(pp \rightarrow h \rightarrow 2h_s \rightarrow 4\mu) = \sigma(pp \rightarrow h) \times B(h \rightarrow h_s h_s) \times [B(h_s \rightarrow \mu^+ \mu^-)]^2, \quad (38)$$

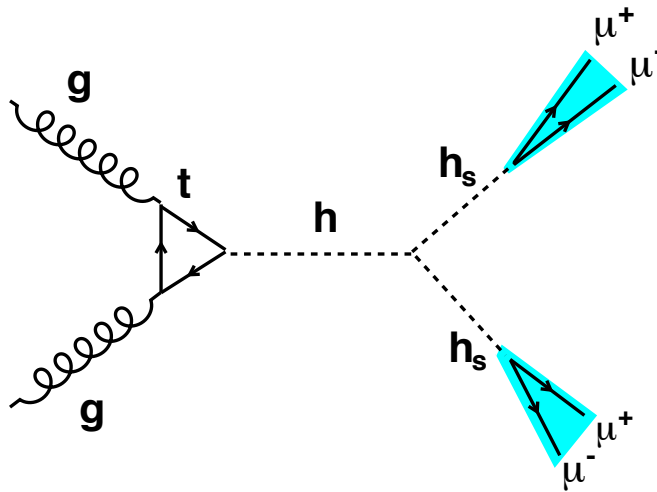


FIG. 2. The Feynman diagram for two  $2\mu$ -jets in the final state for the Higgs-portal Model-1 (SM + one light scalar  $h_s$ ):  $pp \rightarrow h \rightarrow h_s h_s \rightarrow (\mu^+ \mu^-) (\mu^+ \mu^-)$ .

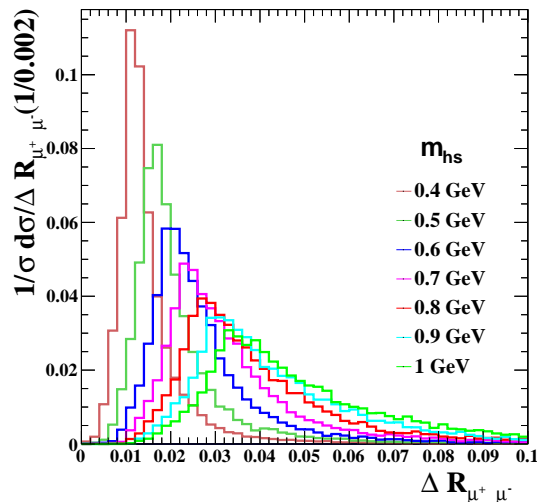


FIG. 3. The opening angle  $\Delta R_{\mu^+ \mu^-}$  distribution for a pair of oppositely-charged muons inside a muon-jet for each benchmark point in the Higgs-portal model-1, at LHC 14 TeV with Delphes ATLAS simulations.

where for 14 TeV  $\sigma(pp \rightarrow h) = 49.97$  pb [19]. Figure 4 shows the distribution of  $\Delta R_{\mu^+ \mu^-}$  versus the invariant mass of the muon pair for each benchmark point in Higgs-portal model-1. We can clearly see that the opening angle for the dimuon pair is of order  $O(0.01)$ . As the mass of  $h_s$  increases the opening angle  $\Delta R_{\mu^+ \mu^-}$  between the two muons becomes wider, because the opening angle roughly scales as  $m_{h_s}/p_{T_{h_s}}$ .

## B. Higgs-portal model-2

### 1. Event Topologies

In the Higgs-portal model-2, there are two light scalars  $h_{D_1}$  and  $h_{D_2}$  in the dark sector. The dominant muon-jet processes come from gluon fusion into the Higgs boson, followed by the Higgs decays into two light scalars:  $h \rightarrow h_{D_1} h_{D_1}$ ,  $h \rightarrow h_{D_1} h_{D_2}$ , and  $h \rightarrow h_{D_2} h_{D_2}$ . Here  $h_{D_1}$  denotes the slightly heavier scalar boson between the two light scalars. The  $h_{D_1}$  can decay into a pair of  $h_{D_2}$ , and we choose  $h_{D_2}$  to decay into a pair of opposite-charged

TABLE II. Signal cross sections, total decay widths, and decay lengths for the process  $pp \rightarrow h \rightarrow 2h_s \rightarrow 4\mu$  for various benchmark points of the Higgs-portal Model-1 at LHC-14. We choose  $m_{h_s} = 0.4 - 1.0$  GeV for various  $\sin\theta$ . Note that the innermost part of the tracker system is the pixel detector, which spans from 1 few cm to about 10 cm. Therefore, it can cover  $m_{h_s} \gtrsim 0.5$  GeV without problems. For lighter  $h_s$  we can use the outside muon spectrometer.

$m_{h_s}$ (GeV)	0.4	0.5	0.6	0.7	0.8	0.9	1.0
$\sin\theta$ ( $10^{-3}$ )	2.83	3.16	3.54	4.08	4.71	8.16	15.8
$\sigma_{14TeV}$ (fb)	43.49	27.84	17.82	10.02	5.64	0.63	0.04
$\Gamma_{h_s}$ ( $10^{-13}$ GeV)	1.13	2.69	5.56	12.2	25.7	267	4250
$\gamma c\tau$ (cm)	27.3	9.2	3.7	1.4	0.6	0.05	0.003

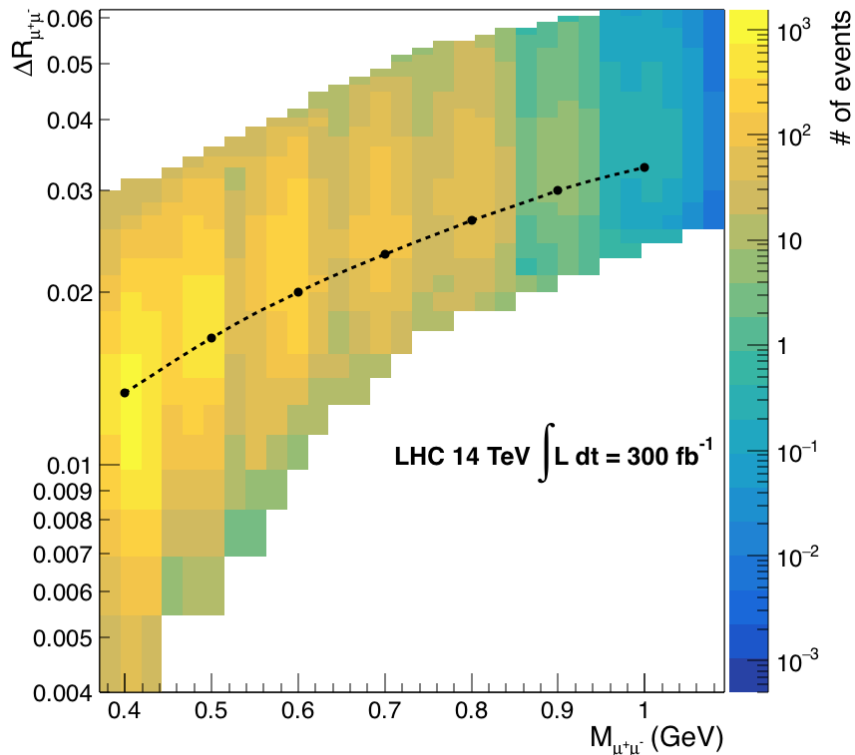


FIG. 4. The opening angle  $\Delta R_{\mu^+\mu^-}$  versus invariant mass  $M_{\mu^+\mu^-}$  for a pair of oppositely-charged muons in the Higgs-portal model-1, at LHC 14 TeV, luminosity  $300fb^{-1}$  with Delphes ATLAS simulations.

muons. Thus we can have 3 final state topologies:

1. TP1: two  $2\mu$ -jets,
2. TP2: one  $2\mu$ -jet and one  $4\mu$ -jet, and
3. TP3: two  $4\mu$ -jets.

The Feynman diagrams for these processes are shown in Fig. 5. The final states corresponding to the event topologies TP1, TP2, and TP3 consist of 4, 6, and 8 muons, respectively, which are organized into two back-to-back muon-jets. Each  $2\mu$ -jet is made up of a pair of oppositely-charged muons while each  $4\mu$ -jet consists of two pair of oppositely-charged muons. The angular separation between the two oppositely-charged muons in each  $2\mu$ -jet depends on the mass of the two light scalars, which is of order  $O(0.01)$  in  $\Delta R_{\mu^+\mu^-}$ . On the other hand, the angular separation

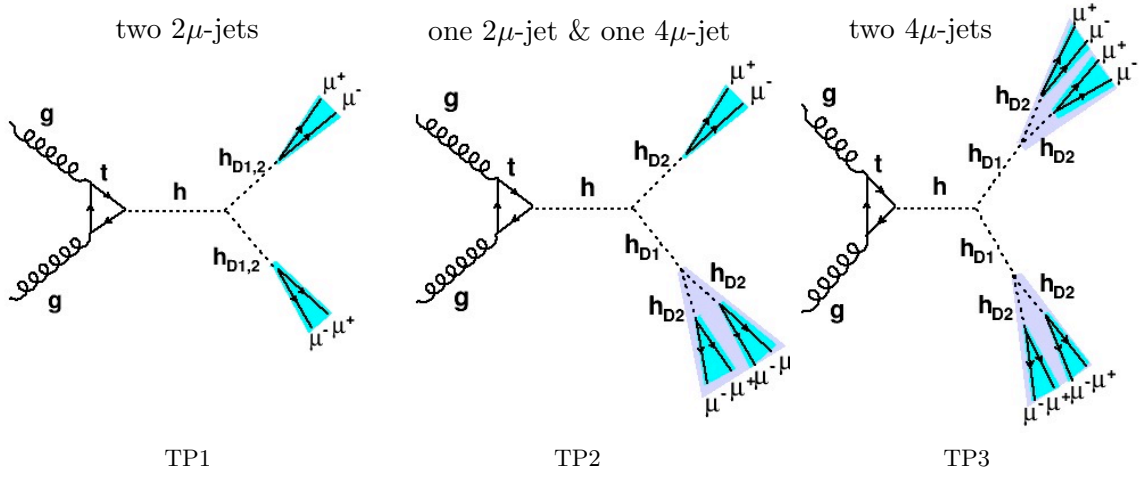


FIG. 5. Feynman diagrams for muon-jet processes with the Higgs-portal model-2: SM + two Light Scalar  $h_{D1}$  and  $h_{D2}$ . Event topologies: (i) TP1:  $pp \rightarrow h \rightarrow h_{D1/2}h_{D1/2} \rightarrow (\mu^+\mu^-) (\mu^+\mu^-)$ ; (ii) TP2:  $pp \rightarrow h \rightarrow h_{D1}h_{D2} \rightarrow (h_{D2}h_{D2})h_{D2} \rightarrow (\mu^+\mu^-\mu^+\mu^-) (\mu^+\mu^-)$ ; (iii) TP3:  $pp \rightarrow h \rightarrow h_{D1}h_{D1} \rightarrow (h_{D2}h_{D2}) (h_{D2}h_{D2}) \rightarrow (\mu^+\mu^-\mu^+\mu^-) (\mu^+\mu^-\mu^+\mu^-)$ . Each pair of parentheses represents a muon-jet.

between the two oppositely-charged muons in each  $4\mu$ -jet has a longer tail because half of the times the wrong pair of muons are grouped together.

TABLE III. Benchmark points for case 1, 2, and 3 of the Higgs-portal model-2.

$m_{h_{D1}}$ (GeV)	case 1		case 2		case 3	
$\sin \theta_1$ ( $10^{-3}$ )	(1)	(2)	(1)	(2)	(1)	(2)
$\Gamma_{h_{D1}}$ ( $10^{-9}$ GeV)						
$m_{h_{D2}}$ (GeV)	0.5	1.0	0.5	1.0	0.5	1.0
$\sin \theta_2$ ( $10^{-3}$ )	3.16	15.8	3.16	15.8	3.16	15.8
$\Gamma_{h_{D2}}$ ( $10^{-13}$ GeV)	2.69	4250	2.69	4250	2.69	4250
$\mu_{HD}$ ( $10^{-3}$ GeV)	1.08	1.33	1.08	1.33	1.08	1.33

The most updated fits to the Higgs boson signal strengths [10] restrict the couplings of  $hh_{D1}h_{D1}$ ,  $hh_{D1}h_{D2}$  and  $hh_{D2}h_{D2}$  by  $\Gamma(h \rightarrow \text{nonstandard}) < 0.94$  MeV or  $B(h \rightarrow \text{nonstandard}) < 19\%$ . Therefore, we choose 3 different cases for different combinations of  $\lambda_{\Phi X}$  and  $\alpha$  as follows:

- case 1 :  $B(h \rightarrow h_{D1}h_{D1}) = B(h \rightarrow h_{D1}h_{D2}) = 4 \cdot B(h \rightarrow h_{D2}h_{D2})$   
 $\lambda_{\Phi X} = 4.66 \times 10^{-3}$  and  $\alpha = \frac{1}{\sqrt{2}}$  ;
- case 2 :  $B(h \rightarrow h_{D1}h_{D1}) = 10 \cdot B(h \rightarrow h_{D1}h_{D2}) = 400 \cdot B(h \rightarrow h_{D2}h_{D2})$   
 $\lambda_{\Phi X} = 6.65 \times 10^{-3}$  and  $\alpha = \frac{1}{2\sqrt{5}}$  ;
- case 3 :  $B(h \rightarrow h_{D1}h_{D1}) = \frac{1}{10} \cdot B(h \rightarrow h_{D1}h_{D2}) = \frac{1}{25} \cdot B(h \rightarrow h_{D2}h_{D2})$   
 $\lambda_{\Phi X} = 1.16 \times 10^{-3}$  and  $\alpha = \sqrt{5}$ .

We list the benchmark points for each case in Table III. We shall also display the  $p_T$  and  $\eta$  distributions of the benchmark points for case 1 with final states of 4, 6, and 8 muons in appendix.

## 2. Simulations

The Higgs-portal model-2 can produce 4, 6, or 8 muons in the final state with event topologies TP1, TP2, and TP3. Since the muons originate from the 125 GeV Higgs boson, the more the muons in the final state, the lower the transverse momentum  $p_{T_\mu}$  for each muon will be. Therefore, we would not get very energetic muons in the final states with multi-muons. The topology TP1 with two  $2\mu$ -jets in the final state suffers from the constraint of the CMS search [15] just like the Higgs-portal model-1. The other two topologies TP2 and TP3 containing one or more  $4\mu$ -jets, each of which is made up of four muons, and so the  $p_T$  of each muon is softer than that of each  $2\mu$ -jet. At the LHC, both ATLAS and CMS experiments can detect collimated and soft muons [15, 20]. In this work, we use the muon detection efficiency for soft muons (muons with  $p_T < 10$  GeV) for ATLAS experiments [21, 22] in the fast detector simulation with Delphes. We use MADGRAPH v.5 [23] with parton showering by Pythia v.6 [24], detector simulations using Delphes v.3 [25, 26], and the analysis tools by MadAnalysis5 [27].

The muon-jet in our Delphes simulation is defined as [20, 28]: Starting with the hardest muon we collected all muons within  $\Delta R = 0.1$  around it and added their 4-vectors to the muon-jet. This was repeated until no further muons were found within  $\Delta R = 0.1$  around the muon-jet 4-vector. This same 4-vector was then used to define the isolation cone  $0.1 < \Delta R < 0.4$ . Here we collected the muon candidates as: within a cone of  $\Delta R < 0.001$  the maximum transverse momenta sum of all charge tracks with  $P_T > 0.5$  GeV but the muon one is  $\sum P_T < 2$  GeV. Then we use kinematic cuts to check if two (or four) muons will survive the  $\Delta R_{\mu^+\mu^-} < 0.3$  (or  $\Delta R_{4\mu} < 1$ ) cut.<sup>4</sup>

We are going to perform simulations for the final-state topologies of TP1, TP2 and TP3 in case 1 of the Higgs-portal model-2. Note that the choice of parameters in case 1 allows all three event topologies. In the Higgs-portal model, the light scalars comes from the Higgs boson decay, thus the Higgs-mass-window cut can be used to separate the signal from backgrounds. We show in the appendix the invariant mass of  $\mu$ -jets for case 1 of the Higgs-portal model-2 to illustrate the Higgs-mass window in three final-state topologies TP1, TP2 and TP3.

## 3. Angular Separation, Invariant mass and Cross Sections

The cross sections for two  $2\mu$ -jets (TP1), one  $2\mu$ -jet & one  $4\mu$ -jet (TP2), and two  $4\mu$ -jets (TP3) are given by

$$\begin{aligned}
 \text{TP1} : & \sigma(pp \rightarrow h \rightarrow 2h_{D1/D2} \rightarrow 4\mu) \\
 & = \sigma(pp \rightarrow h) \times B(h \rightarrow h_{D1/D2}h_{D1/D2}) \times [B(h_{D1/D2} \rightarrow \mu^+\mu^-)]^2 \\
 \text{TP2} : & \sigma(pp \rightarrow h \rightarrow h_{D1}h_{D2} \rightarrow h_{D2}h_{D2}h_{D2} \rightarrow 6\mu) \\
 & = \sigma(pp \rightarrow h) \times B(h \rightarrow h_{D1}h_{D2}) \times B(h_{D1} \rightarrow h_{D2}h_{D2}) \times [B(h_{D2} \rightarrow \mu^+\mu^-)]^3 \\
 \text{TP3} : & \sigma(pp \rightarrow h \rightarrow h_{D1}h_{D1} \rightarrow h_{D2}h_{D2}h_{D2}h_{D2} \rightarrow 8\mu) \\
 & = \sigma(pp \rightarrow h) \times B(h \rightarrow h_{D1}h_{D1}) \times [B(h_{D1} \rightarrow h_{D2}h_{D2})]^2 \times [B(h_{D2} \rightarrow \mu^+\mu^-)]^4
 \end{aligned}$$

The cross sections for three different event topologies for all benchmark points are listed in Table IV. In all three cases of the Higgs-portal model-2, the branching ratio  $B(h_{D1} \rightarrow h_{D2}h_{D2})$  is about 100%. The main difference among the three cases lies in the coupling strengths of  $hh_{D1}h_{D1}$ ,  $hh_{D1}h_{D2}$  and  $hh_{D2}h_{D2}$ .

TABLE IV. Muon-jet cross sections at the LHC-14 for the event topologies TP1: two  $2\mu$ -jets; TP2: one  $2\mu$ -jet & one  $4\mu$ -jet; and TP3: two  $4\mu$ -jets in case 1, 2, and 3.

$\sigma_{14TeV}$ (fb)	case 1		case 2		case 3	
	(1)	(2)	(1)	(2)	(1)	(2)
TP1	10.55	0.017	0.23	$3.58 \times 10^{-4}$	65.93	0.11
TP2	4.18	$2.67 \times 10^{-4}$	0.85	$5.45 \times 10^{-5}$	2.61	$1.67 \times 10^{-4}$
TP3	0.41	$1.06 \times 10^{-6}$	0.84	$2.16 \times 10^{-6}$	0.026	$6.62 \times 10^{-8}$

In Fig. 6, we show the opening angle  $\Delta R_{\mu^+\mu^-}$  distributions for a pair of oppositely-charged muons inside a muon-jet in different final-state event topologies TP1, TP2, and TP3. We show the choice of parameters for case 1 with

<sup>4</sup> For  $4\mu$ -jet reconstruction: (i) we used the angular separation of muon pairs with  $\Delta R_{\mu^+\mu^-}$  smaller than the proper cone size ( $\Delta R_{\mu^+\mu^-} \sim 2m_{h_s}/P_{T_{h_s}}$  for directly decaying  $2\mu$ -jet), (ii) find two oppositely charged muons within a  $\Delta R$  cone with an invariant mass peaked at the lighter scalar-boson mass to reconstruct a  $2\mu$ -jet, (iii) then find a pair of these  $2\mu$ -jets within the  $\Delta R$  cone, with an invariant mass peaked at the heavier scalar-boson mass to reconstruct the  $4\mu$ -jet.

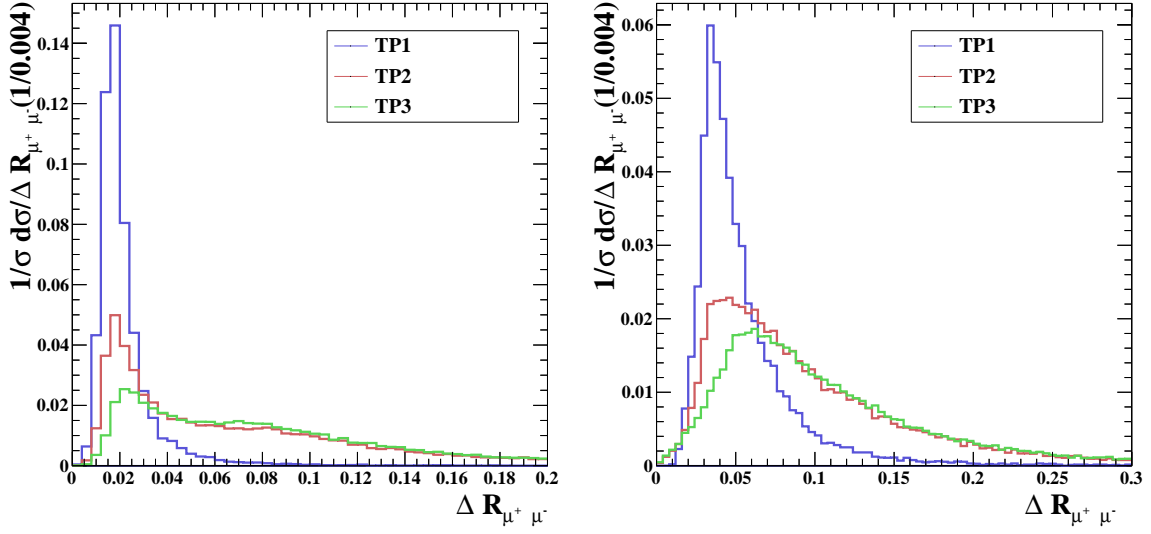


FIG. 6. The opening angle  $\Delta R_{\mu^+\mu^-}$  distributions for a pair of oppositely-charged muons inside a muon-jet. We show the choice of parameters for case 1 in the Higgs-portal model-2 with  $m_{h_{D_1}} = 2.5$  GeV and  $m_{h_{D_2}} = 0.5$  (left), 1.0 GeV (right). At LHC 14 TeV with Delphes ATLAS simulations.

$m_{h_{D_1}} = 2.5$  GeV and  $m_{h_{D_2}} = 0.5/1.0$  GeV. We can see the cone sizes of all the TP1, TP2 and TP3 are within the order  $O(0.1)$ . For each  $2\mu$ -jets there is only one pair of oppositely-charged muons in the jet cone, and so the angular separation  $\Delta R_{\mu^+\mu^-}$  will enlarge with increases in the mass. For each  $4\mu$ -jet there are two pairs of oppositely-charged muons inside the jet cone, and therefore the  $4\mu$ -jet is "fatter" than the  $2\mu$ -jet. The event topology TP2 can come from the Higgs decay into  $h_{D_1}$  and  $h_{D_2}$ . We can see that the  $\Delta R_{\mu^+\mu^-}$  distribution has a sharp peak plus a long tail. The sharp peak comes from the decay  $h_{D_2} \rightarrow \mu^+\mu^-$ , which coincides with the first peak of TP1. On the other hand, the long tail comes from the decay  $h_{D_1} \rightarrow h_{D_2}h_{D_2} \rightarrow \mu^+\mu^-\mu^+\mu^-$ , for which half of the times the wrong pair of oppositely-charged muons are grouped together.

## V. SENSITIVITY REACH AT THE LHC

The most important question is how many events for this kind of nonstandard decays of Higgs boson that the LHC-14 with  $300fb^{-1}$  can probe via these collimated muon-jet objects. Since these topologies in the final state have very little background, we shall estimate the background event rates after applying successive levels of cuts, and then calculate the signal event rates at 95% CL. For detector efficiencies of these multimMuon-jets final states, we follow Ref. [29] for the non-prompt decay of light scalar bosons.

The major background after selection cuts dominantly comes from the charmonium and bottomonium production. Multiple muons can come off cascade semileptonic or leptonic decays, which are taken as non-prompt. There could easily be 4 or more muons in the final state. On the other hand, multiple muons which come from the low-mass Drell-Yan process  $pp \rightarrow Z/\gamma^* \rightarrow 4\mu$  and the one via Higgs boson production  $pp \rightarrow h \rightarrow ZZ^* \rightarrow 4\mu$  and even  $t\bar{t}$  production are taken as prompt. They are totally suppressed by the selection cuts. The event rates for various backgrounds are very low. We shall show them momentarily.

In Ref. [29], the ATLAS Collaboration searched for lepton-jets in the 8 TeV data with a luminosity of  $20.3fb^{-1}$  in two different FRVZ models [1], which predict non-SM Higgs boson decays into lepton-jets. The process for the first model is

$$h \rightarrow f_{d_2}f_{d_2} \rightarrow (\gamma_d HLSP)(\gamma_d HLSP) \rightarrow (l^+l^-)HLSP(l^+l^-)HLSP.$$

where  $f_{d_2}$ ,  $\gamma_d$  and  $HLSP$  are the hidden fermion, the dark photon and the hidden lightest stable particle in the first FRVZ model. The final state of this model consists of two  $2\mu$ -jets + mET. The process for the second model is

$$\begin{aligned} h \rightarrow f_{d_2}f_{d_2} \rightarrow (s_{d_1} HLSP)(s_{d_1} HLSP) \rightarrow (\gamma_d \gamma_d)HLSP(\gamma_d \gamma_d)HLSP \\ \rightarrow (l^+l^-)(l^+l^-)HLSP(l^+l^-)(l^+l^-)HLSP. \end{aligned}$$

where  $s_{d_1}$  is the hidden scalar in the second FRVZ model. The final state of this model is two  $4\mu$ -jets + mET.

In the first model, for  $m_{\gamma_d} = 0.4 - 0.9$  GeV, the reconstruction efficiency of muon-jets as a function of the transverse momentum  $p_T$  and the transverse decay distance  $L_{xy}$  of the  $\gamma_d$  for the  $2\mu$ -jet is about 9% – 12%. In the second model, for  $m_{s_{d_1}} = 2$  GeV and  $m_{\gamma_d} = 0.4 - 0.9$  GeV, the reconstruction efficiency of muon-jets as a function of  $p_T$  of the  $s_{d_1}$  for the  $4\mu$ -jet is about 17% – 20%. Finally, the muon trigger efficiency for  $m_{\gamma_d} = 0.4 - 0.9$  GeV as a function of  $p_T$  of the  $\gamma_d$  for  $\gamma_d \rightarrow \mu^+\mu^-$  is about 40%. Note that triggering the event by seeing at least *one muon* is enough.

Since the final states of our Higgs-portal models are similar to these two FRVZ models except for the mET, we will use the relevant reconstruction efficiencies and muon trigger efficiency to simply estimate the detector efficiencies for the non-prompt decay of light scalar bosons. For the reconstruction efficiencies, we use 10% for the  $2\mu$ -jet case and 20% for the  $4\mu$ -jet case for our benchmark points. For the muon trigger efficiency, we also use 40% for both  $h_s \rightarrow \mu^+\mu^-$  and  $h_{D_2} \rightarrow \mu^+\mu^-$ . We summarize the detector efficiencies for different topologies TP1, TP2 and TP3 as follows

$$\begin{aligned} \text{TP1} : \epsilon &\approx (10\%)^2 \times [1 - (1 - (40\%))^4] = 8.7 \times 10^{-3} \\ \text{TP2} : \epsilon &\approx (10\%) \times (20\%) \times [1 - (1 - (40\%))^6] = 0.019 \\ \text{TP3} : \epsilon &\approx (20\%)^2 \times [1 - (1 - (40\%))^8] = 0.039 \end{aligned}$$

We first look at the Higgs-portal model-1 with only one light scalar  $h_s$ . The scalar  $h_s$  can decay into a pair of collimated muons. Therefore, the final state consists of two  $2\mu$ -jets, corresponding to the topology TP1. We show the observable events in Table V for benchmark points in Table II at LHC-14 with  $300fb^{-1}$ . The number of events decreases gradually from 114 at  $m_{h_s} = 0.4$  GeV down to 2 at  $m_{h_s} = 0.9$  GeV, which is mainly because of the decrease in branching ratio  $B(h_s \rightarrow \mu^+\mu^-)$  (see Table I). Note that the decay lengths of  $h_s$  for  $m_{h_s} = 0.4 - 0.9$  GeV are longer than the criterion of prompt decay length (0.15 mm), and so we use detector efficiencies of non-prompt decay for  $m_{h_s} = 0.4 - 0.9$  GeV. However, for  $m_{h_s} = 1.0$  GeV the decay length is shorter than 0.15 mm and thus considered prompt decay, and we use the efficiencies for prompt decays.<sup>5</sup> The number of events rises to 6 for  $m_{h_s} = 1.0$  GeV.<sup>6</sup>

TABLE V. Number of events for the process  $pp \rightarrow h \rightarrow 2h_s \rightarrow 4\mu$  of the Higgs-portal model-1 at LHC-14 with  $300fb^{-1}$  for benchmark points in Table II.

$m_{h_s}$ (GeV)	0.4	0.5	0.6	0.7	0.8	0.9	1.0
# of events	114	73	47	26	15	2	6

Next we consider the Higgs-portal model-2. Since the number of parameters involved are many, we first fix  $\mu_{HD}$  which controls the branching ratio  $B(h_{D_1} \rightarrow h_{D_2}h_{D_2})$ . The branching ratio  $B(h_{D_1} \rightarrow h_{D_2}h_{D_2})$  is shown in Fig. 7 for fixed  $m_{h_{D_2}} = 2.5$  GeV with various values of  $\mu_{HD}$ . For  $\mu_{HD} = (1.0 - 1.5) \times 10^{-3}$  the branching ratio is almost above 0.99 in the mass range shown.

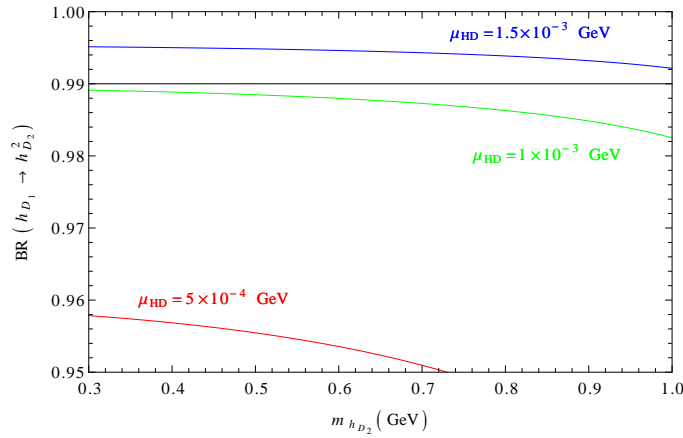


FIG. 7. The branching ratio  $B(h_{D_1} \rightarrow h_{D_2}h_{D_2})$  versus  $m_{h_{D_2}}$  for various  $\mu_{HD}$  with fixed  $m_{h_{D_2}} = 2.5$  GeV. The purpose of the graph is to show how large  $\mu_{HD}$  is required to give a branching ratio larger than 0.99 for  $m_{h_{D_2}} = 2.5$  GeV.

<sup>5</sup> Since the efficiencies for the decay length around 0.15 mm between non-prompt and prompt decays are a complicated continuous function, here we just want to simply show the major differences of numerical values between these two kinds of efficiencies.

<sup>6</sup> We used the same selection cuts as in Table VII for calculation of the efficiencies for prompt decays with Delphes, and got  $\epsilon = 0.460$ .

The topology TP2 (one  $2\mu$ -jet and one  $4\mu$ -jet) and topology TP3 (two  $4\mu$ -jets) can come from case 1, 2 and 3 of the Higgs-portal model-2. We show the observable events in Table VI for benchmark points in Table III at LHC-14 with  $300fb^{-1}$ . Here we only show number of events larger than 1. <sup>7</sup>

TABLE VI. Number of events for TP1, TP2 and TP3 of Higgs portal model-2 at LHC-14 with  $300fb^{-1}$  for benchmark points in Table III.

# of events	case 1		case 2		case 3	
	(1)	(2)	(1)	(2)	(1)	(2)
TP1	28	2	1	–	172	15
TP2	24	–	5	–	15	–
TP3	5	–	10	–	–	–

TABLE VII. Number of background events for TP1, TP2 and TP3 at LHC-14 with  $300fb^{-1}$ .

Cuts/# of BG events	TP1	TP2	TP3
$N(\mu) = 4, (6, 8)$	485452	236522	82104
$p_{T_\mu} > 5GeV$	50667	34724	15138
$ \eta_\mu  < 2.4$	50667	34724	15138
$p_{T_{\mu_1}} > 20GeV$	23873	17441	7936
$115GeV <  M_{\sum \mu_i}  < 135GeV$	28	59	28
$M_{2\mu} < 3GeV, \Delta R_{2\mu} < 0.3$	8.49	21.22	
$M_{4\mu} < 3GeV, \Delta R_{4\mu} < 1$			27.59

We perform background calculations for 4, 6, 8 muons to form muon-jets under successive cuts. The charmonium and bottomonium are the dominant backgrounds. We start with  $3.18 \times 10^6$  events (corresponding to the background cross section with  $300fb^{-1}$ ), and show the subsequent numbers after each level of cuts in Table VII. At the end of the cut flow, the number of background events remaining are 8.49, 21.22 and 27.59 for TP1, TP2, and TP3, respectively. Thus, the 95%CL upper limits (roughly  $Z = 2$ ) <sup>8</sup> for signal event numbers are 6.46, 9.86, 11.15, respectively. We then use these signal event rates to show the sensitivity reach in the parameter space.

We can now compare the sensitivity reach by the topologies TP1, TP2, and TP3. The more muons to be seen, the higher the price has to be paid for detection efficiency. Nevertheless, the signature of one  $2\mu$ -jet and one  $4\mu$ -jet in the final state is one of the most striking decays of the Higgs boson that we can imagine. It implies the existence very light particles involved in the decay chain. Similarly, two  $4\mu$ -jets in the final state also signal multiple light scalar bosons in the dark sector.

First, we start from the Higgs-portal model-1. After adding all the constraints described in Sec. III shown in Fig. 1, we can further use the 95%CL upper limits (roughly  $Z = 2$ ) in our analysis of LHC-14 with  $300fb^{-1}$  to show the sensitivity reach for  $\langle\chi\rangle = 10$  GeV and for  $\langle\chi\rangle = 100$  GeV in Fig. 8. Note that in Fig. 8 the orange and yellow regions show beyond the limit of the displaced muon reconstruction for decay length for ATLAS and CMS, respectively. The gray hatched region is where our analysis can cover. We can see from these figures, LHC-14 with  $300fb^{-1}$  in our analysis could cover all the parameter space of  $m_{h_s} < 0.5$  GeV within possible muon reconstruction inside the detectors.

While the parameter space in the plane of  $\log_{10} \sin^2 \theta$  vs  $m_{h_s}$  for the Higgs-portal model-1 depends on the choice of  $\langle\chi\rangle$ , we can also show the parameter space in the plane of  $\log_{10} |\lambda_{\Phi X}|$  vs  $m_{h_s}$  in Fig. 9, which is independent of the choice of  $\langle\chi\rangle$ . <sup>9</sup> This plot can allow us to have more direct comparison with the plots for Higgs-portal model-2.

Next we can use the similar approach to show the parameter space in the plane of  $\log_{10} |\lambda_{\Phi X}|$  vs  $m_{h_{D_2}}$  for case 1, 2 and 3 in the Higgs-portal model-2 in Fig. 10. An interesting observation is that there are some crossovers among

<sup>7</sup> Similarly, We also used the same selection cuts as in Table VII for calculation of the efficiencies for prompt decays with Delphes to TP1, TP2, and TP3, and got  $\epsilon = 0.46$  for TP1,  $\epsilon = 0.194$  for TP2, and  $\epsilon = 0.145$  for TP3.

<sup>8</sup> The signal significance  $Z$  defined as

$$Z = \sqrt{2 \cdot ((s+b) \cdot \ln(1+s/b) - s)}, \quad (39)$$

where  $s$  and  $b$  are the expected number of signal and background events, respectively.

<sup>9</sup> The fundamental parameters in the Higgs-portal model-1 are  $\lambda$ ,  $\lambda_X$ ,  $\lambda_{\Phi X}$ ,  $\langle\phi\rangle$ , and  $\langle\chi\rangle$ .  $\theta$  can be derived from these fundamental parameters.

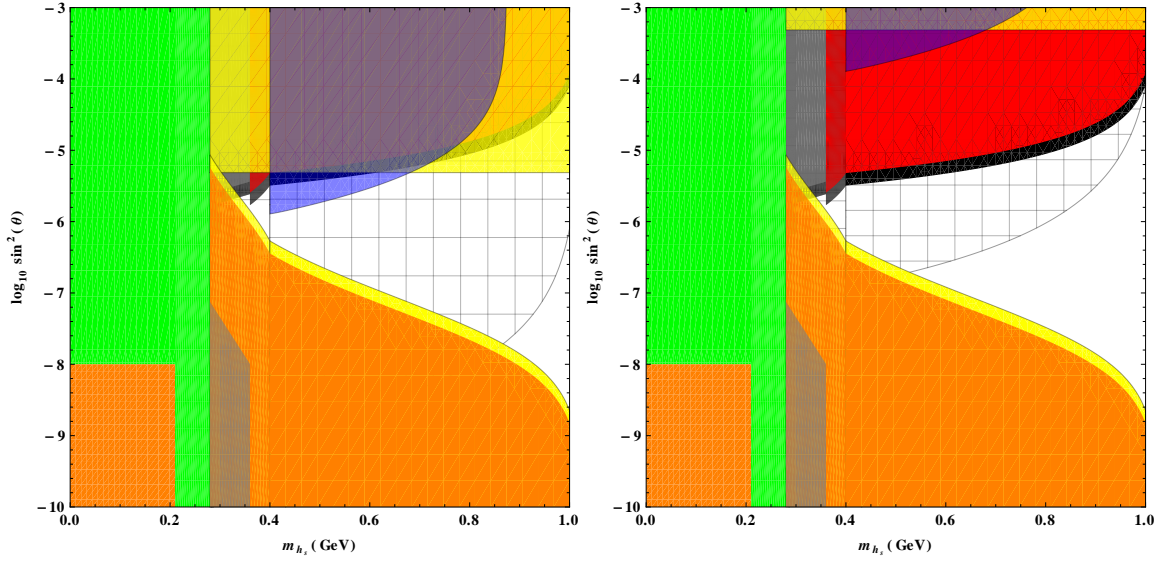


FIG. 8. Similar to Fig. 1, but adding the first constraint in the upper yellow region and third constraint in the upper blue region. We also use the hatched region to display the 95%CL upper limits (roughly  $Z = 2$ ) in our analysis of LHC-14 with  $300 \text{ fb}^{-1}$  to show the sensitivity reach for  $\langle \chi \rangle = 10 \text{ GeV}$  (left panel) and  $\langle \chi \rangle = 100 \text{ GeV}$  (right panel), respectively.

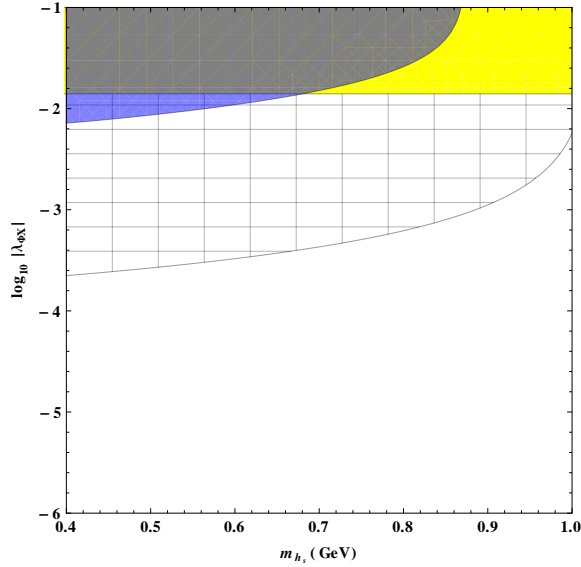


FIG. 9. Existing constraints and the sensitivity reach of LHC-14 with  $300 \text{ fb}^{-1}$  for the Higgs-portal model-1 in the plane of  $\log_{10} |\lambda_{\Phi X}|$  vs  $m_{h_{D_2}}$ . The yellow region is from the first constraint, the blue region is from the third constraint, and the hatched shading lines is to display the 95%CL upper limits (roughly  $Z = 2$ ) in our analysis of LHC-14 with  $300 \text{ fb}^{-1}$ .

different hatched regions in the figure of case 2. To further explore this property, we fix  $m_{h_{D_2}} = 0.5 \text{ GeV}$  and vary different values of  $|\alpha|$  in the plane of  $\log_{10} |\lambda_{\Phi X}|$  vs  $|\alpha|$  in Fig. 11. We can see when  $|\alpha| \lesssim 0.18$  the best sensitivity reach of LHC-14 with  $300 \text{ fb}^{-1}$  is using the TP3 topology, then in the range of  $0.18 \lesssim |\alpha| \lesssim 0.24$  turns out to be TP2, finally after  $|\alpha| \gtrsim 0.24$  the best reach is given by TP1. Such a feature can also be observed for other values of  $m_{h_{D_2}}$ . Another observation is that when  $|\alpha|$  becomes small, the constraint on  $|\lambda_{\Phi X}|$  will also be less stringent.

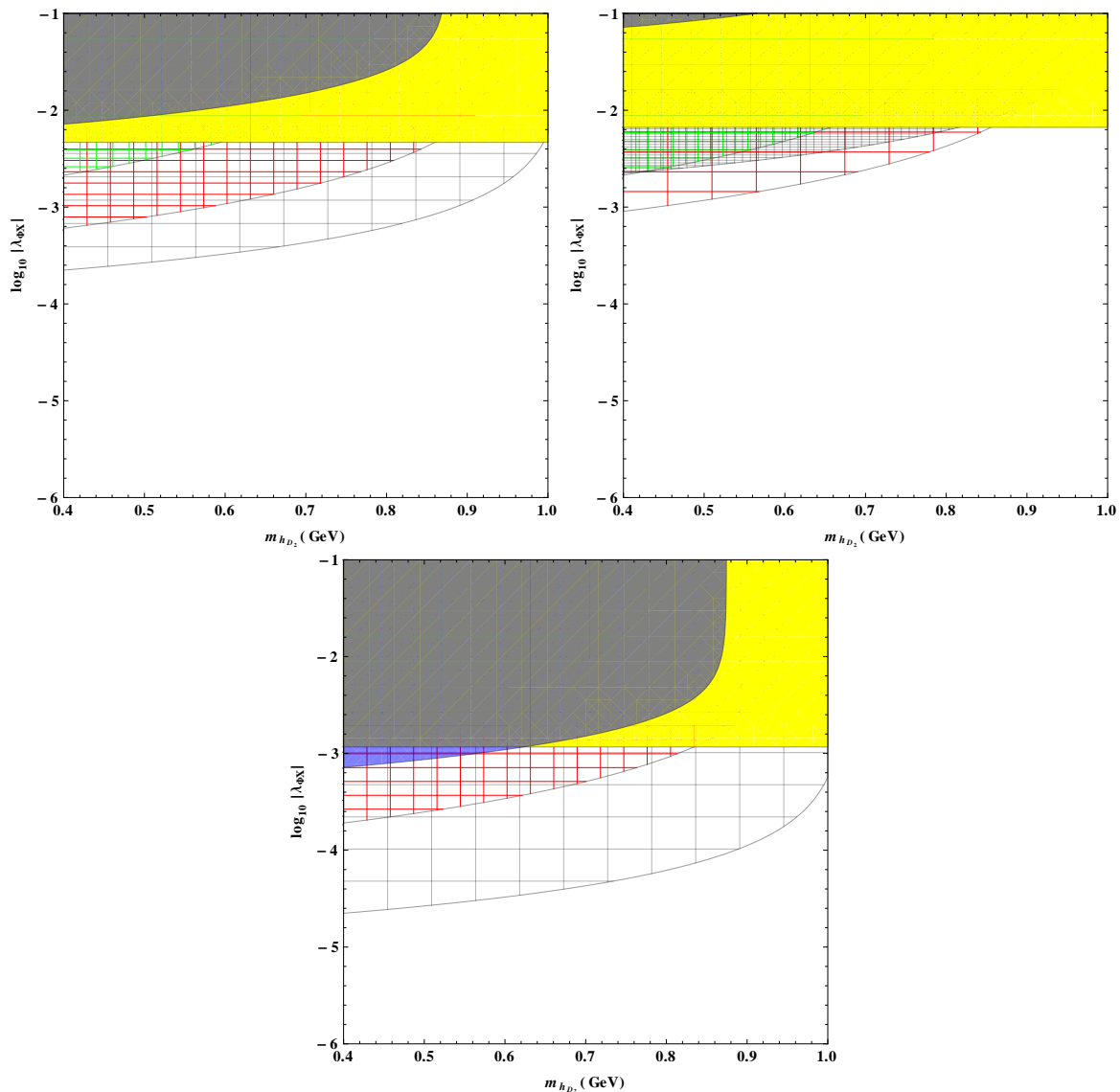


FIG. 10. Existing constraints and the sensitivity reach of LHC-14 with  $300 \text{ fb}^{-1}$  for the Higgs-portal model-2 in the plane of  $\log_{10} |\lambda_{\Phi X}|$  vs  $m_{h_{D_2}}$  for case 1 (upper left panel), case 2 (upper right panel), and case 3 (lower panel). The yellow region is from the first constraint, the blue region is from the third constraint, and the hatched shading lines are to display the 95%CL upper limits (roughly  $Z = 2$ ) in our analysis of LHC-14 with  $300 \text{ fb}^{-1}$  for TP1 (Blue), TP2 (Red), and TP3 (Green).

## VI. CONCLUSIONS

Muon-jets are interesting and clean signatures at colliders, provided the angular resolution of muons are fine enough to differentiate them. The current designs of the ATLAS and CMS have such capabilities of probing angular separation as small as  $10^{-3}$ . In general, muon-jets arise from the decay of fast-moving light particles. In this work, we have demonstrated a couple of dark-sector models, in which there are a number of very light scalar bosons, which can be accessed via the Higgs boson decays. We have investigated the signatures of  $2\mu$ -jets and  $4\mu$ -jets, which consist of, respectively, one and two pairs of oppositely-charged muons in a very narrow cone defined by  $\Delta R \lesssim 0.01$ .

In the Higgs-portal model-1 that we considered, the final state consists of two  $2\mu$ -jets. The current experimental search for such a final state has put on it a tight constraint, such that the allowable cross section becomes very small. On the other hand, in the Higgs-portal model-2 that we considered the final-state event topologies can have (i) two  $2\mu$ -jets (TP1), (ii) one  $2\mu$ -jet and one  $4\mu$ -jet (TP2), or (iii) two  $4\mu$ -jets (TP3). Even though the topologies TP2 and TP3 are still not yet fully constrained from either ATLAS or CMS, their allowable cross sections are yet small. We have also looked at the invariant mass and the angular separation of the oppositely-charged muon pair, which show

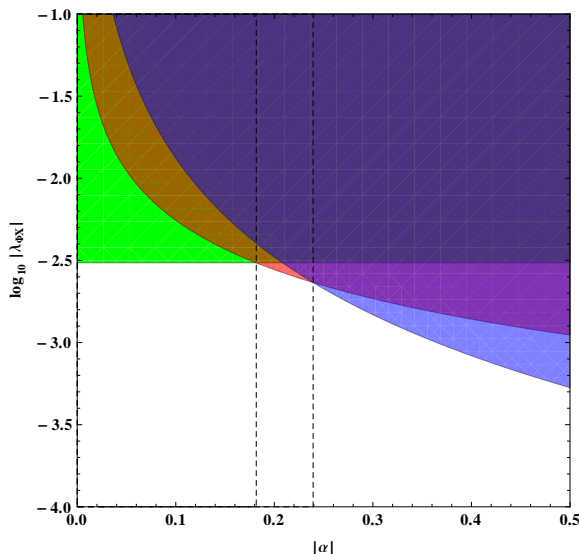


FIG. 11. The sensitivity reach of LHC-14 with  $300 \text{ fb}^{-1}$  for the Higgs-portal model-2 in the plane of  $\log_{10} |\lambda_{\Phi X}|$  vs  $|\alpha|$  with  $m_{h_{D_2}} = 0.5 \text{ GeV}$ . The color regions are to display the 95%CL upper limits (roughly  $Z = 2$ ) in our analysis of LHC-14 with  $300 \text{ fb}^{-1}$  for TP1 (Blue), TP2 (Red), and TP3 (Green).

interesting features that can help distinguishing various topologies. Thus, it helps to pin down the masses of the underlying light scalar bosons.

Before we close we offer the following comments.

1. Since the topologies TP2 and TP3 still allow sizeable cross sections and almost background free, we encourage our experimental groups to focus on these kind of final states and these results will let us know more about the structure of more general dark sector.
2. For the Higgs-portal model-2, if we use much heavier  $h_{D_1}$ , say  $m_{h_{D_1}} \gtrsim 10 \text{ GeV}$ , then we will just see some very collimated muon pairs instead of a "fat" muon-jet without substructure inside it. So it is more interesting to analyze both  $h_{D_1}$  and  $h_{D_2}$  are of mass about  $\mathcal{O}(1 \text{ GeV})$ .
3. For the Higgs-portal model-2, if  $m_{h_{D_2}} < m_{h_{D_1}} < 2m_{h_{D_2}}$ , then  $h_{D_1}$  can decay into  $4\mu$ -jet by one on-shell and one off-shell  $h_{D_2}$  which will have different substructure inside  $4\mu$ -jet from the case of  $m_{h_{D_1}} > 2m_{h_{D_2}}$ , but its cross section is also suppressed.
4. In this work we just investigated the signatures of  $2\mu$ -jets and  $4\mu$ -jets for three different final-state event topologies. However, if we take into account the three-body decay of  $h \rightarrow h_{D_{1/2}} h_{D_{1/2}} h_{D_{1/2}}$  and  $h_{D_1} \rightarrow h_{D_2} h_{D_2} h_{D_2}$ , then we will have more different final-state event topologies, including  $6\mu$ -jets, which can enrich the analysis but are seriously suppressed by the phase space.
5. Our simple models are quite generic for any more complicated models, which include either one or more very light scalar bosons mixing with the SM Higgs boson. There are at least one long-lived neutral particle(s) in this kind of models, which are still testable below  $1 \text{ GeV}$  for both the ATLAS and CMS as shown in Fig. 1. Therefore, we encourage our experimental groups to perform the analysis of real detector effects of the displaced muon reconstruction efficiency of this kind of scenario to further confirm this possibility.

We have demonstrated that the existence of muon-jets such as  $2\mu$ -jets or  $4\mu$ -jets would signal the presence of very light scalar bosons, perhaps coming from dark sectors. We therefore suggest our experimental colleagues to look into the  $n\mu$ -jets with  $n > 2$ . The findings of such objects are definitely signals of new physics and help us to understand the dark sector connecting to the Higgs sector.

## Appendix A: Kinematical Distributions

Here we collect all the kinematical distributions for model-1 and model-2

## 1. Higgs-portal model-1

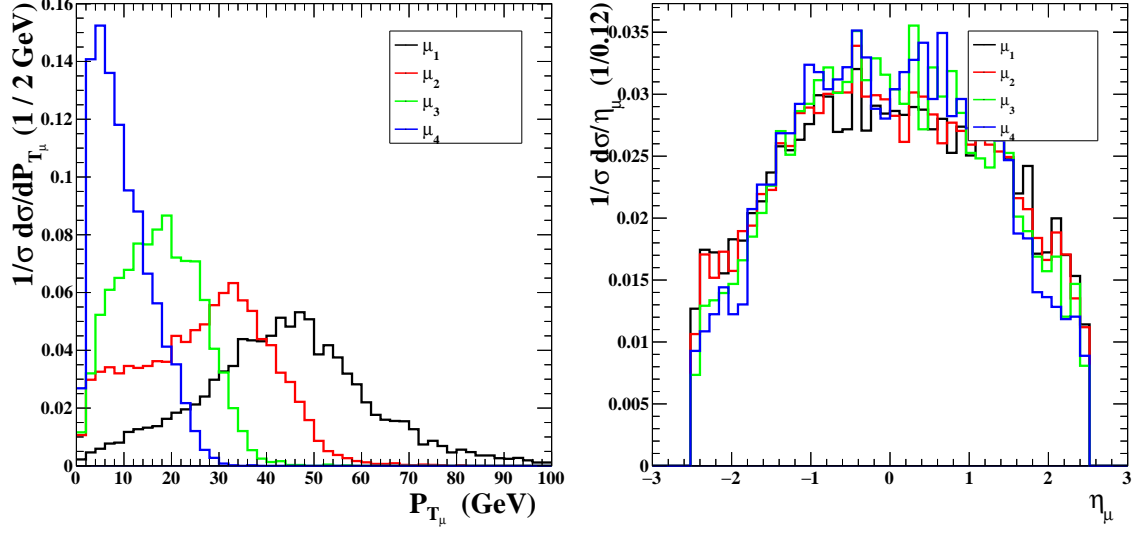


FIG. 12. Transverse momentum  $p_{T_\mu}$  (left panel) and rapidity  $\eta_\mu$  (right panel) distributions for the four final state muons arranged in  $p_T$  in the Higgs-portal model-1 at LHC-14,  $m_{h_s}=0.5$  GeV, at LHC 14 TeV with Delphes ATLAS simulations.

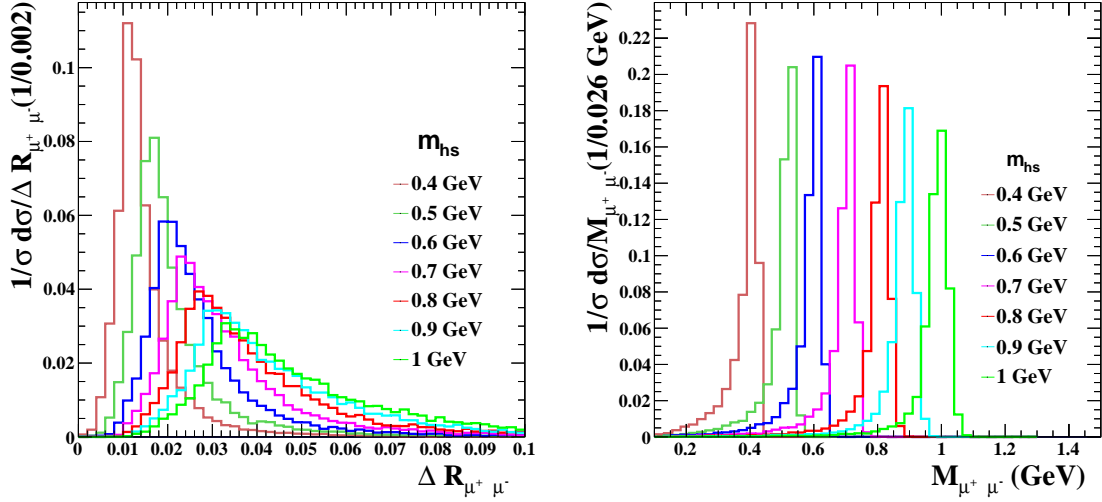


FIG. 13. The opening angle  $\Delta R_{\mu^+\mu^-}$  (left panel) and the invariant mass distribution  $M_{\mu^+\mu^-}$  (right panel) for a pair of oppositely-charged muons inside a muon-jet for each benchmark point in the Higgs-portal model-1, at LHC 14 TeV with Delphes ATLAS simulations.

In the Higgs-portal model-1, there is only one light scalar boson in the dark sector. We display the benchmark point  $m_{h_s}=0.5$  GeV to show the  $p_T$  and  $\eta$  distributions in Fig. 12 for the final state of two  $2\mu$ -jets, and the invariant mass distribution  $M_{\mu^+\mu^-}$  and the opening angle  $\Delta R_{\mu^+\mu^-}$  for a pair oppositely-charged muons inside a muon-jet in Fig. 13 for each benchmark point.

## 2. Higgs-portal model-2

We have explained the various event topologies in the current work and they are

1. TP1: two  $2\mu$ -jets,
2. TP2: one  $2\mu$ -jet and one  $4\mu$ -jet, and
3. TP3: two  $4\mu$ -jets.

Note that the choice of parameters in case 1 allows all three event topologies. We show the  $p_{T\mu}$  and  $\eta_\mu$  distributions for TP1, TP2, and TP3 using the case 1 parameters for the Higgs-portal model-2 in Fig. 14. In the Higgs-portal model, the light scalars comes from the Higgs boson decay, thus the Higgs-mass-window cut can be used to separate the signal from backgrounds. In Fig. 15, we show the invariant mass of  $\mu$ -jets for case 1 of the Higgs-portal model-2 to illustrate the Higgs-mass window in three final-state topologies TP1, TP2 and TP3.

In Fig. 16, we show the invariant mass distribution  $M_{\mu^+\mu^-}$  for a pair of oppositely-charged muons inside a muon-jet in different final-state event topologies TP1, TP2, and TP3. We show the choice of parameters for case 1 with  $m_{h_{D_1}} = 2.5$  GeV and  $m_{h_{D_2}} = 0.5/1.0$  GeV. The invariant mass distributions in each case shown in Fig. 16 clearly show the mass peaks of the light dark scalars for different topologies. For final-state topologies TP2 and TP3 the  $h_{D_1}$  will mostly decay into  $h_{D_2}h_{D_2}$ , and so we can only see one mass peak at  $m_{h_{D_2}}$  plus a long tail because half of the times a wrong pair of oppositely-charged muons are group together.

### Appendix B: Some detailed information about detectors

The pixel detector of ATLAS or CMS is made up of a few layers of silicon pixels organized at radii of about a few cm to about 10 cm [18]. The spatial resolution of the pixels ranges from 10 – 100 $\mu$ m depending on direction. Taking conservatively 100 $\mu$ m as the spatial resolution and divide it by the radius of the tracker, the angular resolution is of order 100 $\mu$ m/10cm  $\sim 10^{-3}$ . This resolution is already better than the angle 0.01 that we estimated above, so that the pixel detector can separate the very collimated muon-jet that we consider in this work. However, there is no guarantee that the pattern recognition algorithms would be able to reconstruct two distinct tracks, especially in the presence of large number of pile-up events.

Besides the inner pixel detector, the muon spectrometer is also very important to identify and measure the momentum of muons. The design of muon spectrometer in ATLAS and CMS is different. The *Muon Spectrometer* of ATLAS is large in size but low in magnetic field. The advantages of this kind of design are its excellency in stand-alone capabilities and safer for high multiplicities. Thus, the ATLAS muon detector performance is excellent over the whole  $\eta$  range and its resolution is nearly constant with  $\eta$ . On the other hand, the CMS muon spectrometer is smaller in size but high in magnetic field. The advantages of this kind of design are its superior combined momentum resolution in the central region and muons can be tracked and pointed back to the primary vertex. Therefore, the CMS muon performance driven by the tracker is better near  $\eta \sim 0$ . We specifically describe the ATLAS muon spectrometer in the following. It is an extremely large tracking system, consisting of three parts: (i) a magnetic field provided by three toroidal magnets, (ii) a set of 1200 chambers measuring with high spatial precision the tracks of the outgoing muons, and (iii) a set of triggering chambers with accurate time-resolution. The extent of this sub-detector starts at a radius of 4.25 m close to the calorimeters out to the full radius of the detector (11 m). Its tremendous size is required to accurately measure the momentum of muons, which first go through all the other elements of the detector before reaching the muon spectrometer. It was designed to measure, stand-alone, the momentum of 100 GeV muons with 3% accuracy and of 1 TeV muons with 10% accuracy. It also serves the function of simply identifying muons – very few particles of other types are expected to pass through the calorimeters and subsequently leave signals in the Muon Spectrometer.

### ACKNOWLEDGEMENT

This work was supported the MoST of Taiwan under Grants No. NSC 102-2112-M-007-015-MY3 and MOST 105-2112-M-007-028-MY3. S.C.H. is supported in parts by the National Science Foundation.

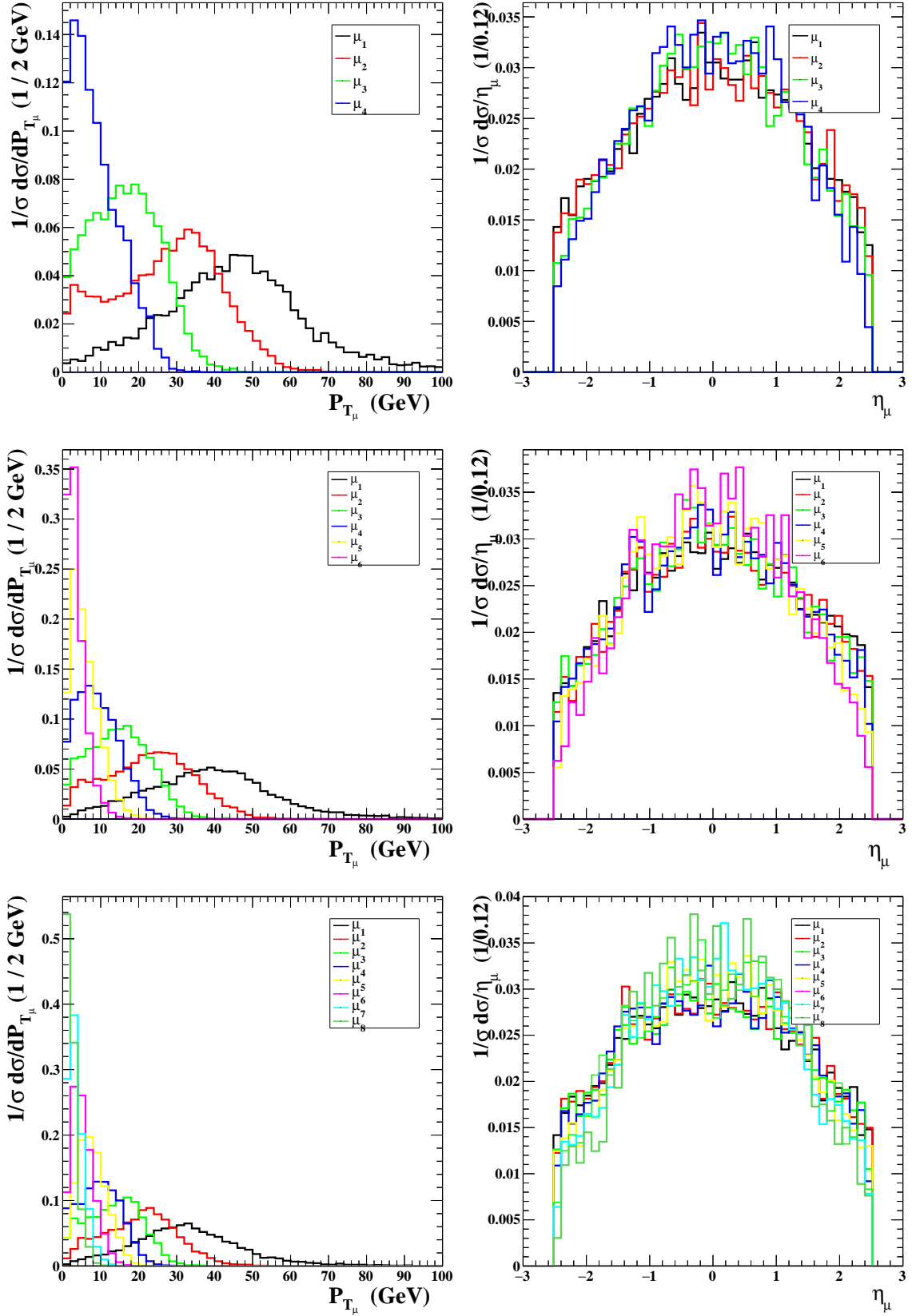


FIG. 14. In the left panels: the  $p_{T\mu}$  distributions with the parameters of case 1, and  $m_{h_{D_1}}=2.5 \text{ GeV}$ ,  $m_{h_{D_2}}=0.5 \text{ GeV}$  for final state topologies of TP1(upper), TP2(medium), and TP3(bottom) with muons arranged in  $p_T$ . In the right panels : the corresponding  $\eta$  distributions. At LHC 14 TeV with Delphes ATLAS simulations.

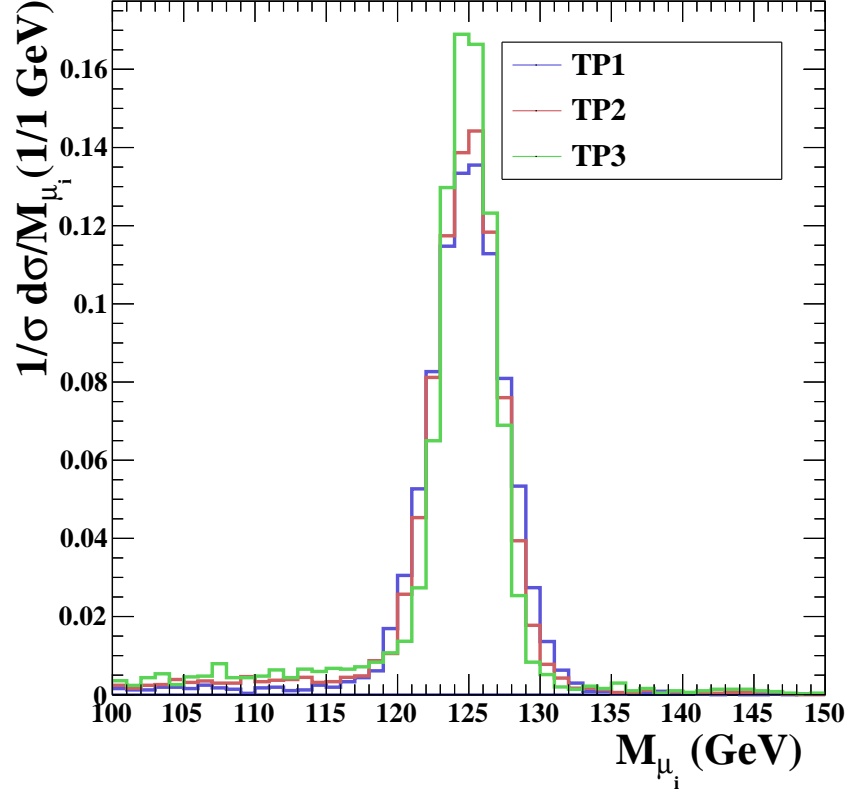


FIG. 15. The invariant mass distribution for the muon-jets, illustrated for the Higgs-portal model-2, case 1:  $m_{h_{D_1}} = 2.5$  GeV,  $m_{h_{D_2}} = 1.0$  GeV, at LHC 14 TeV with Delphes ATLAS simulations.

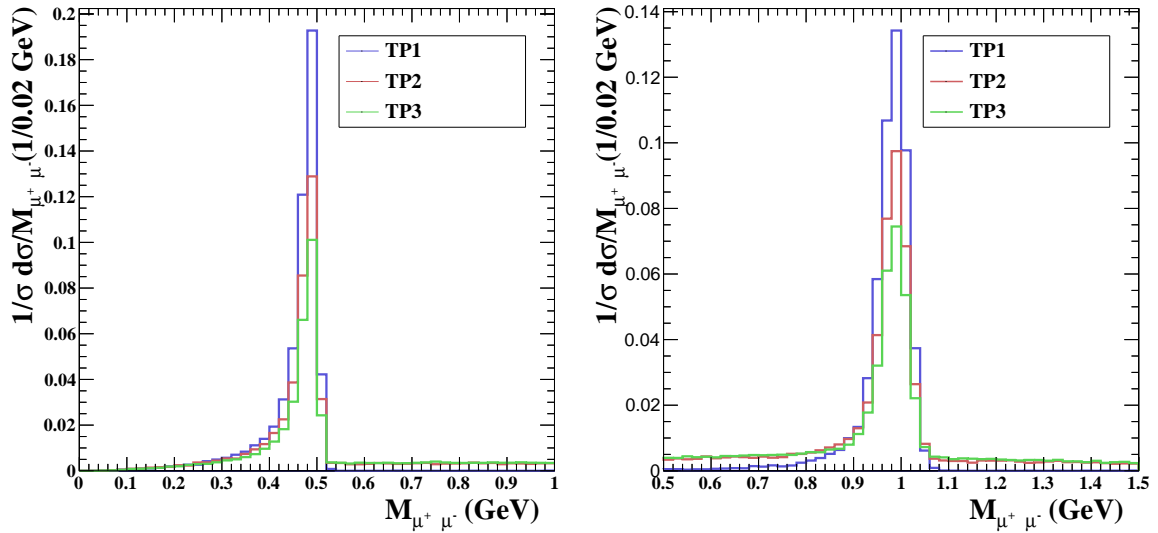


FIG. 16. The invariant mass distribution  $M_{\mu^+ \mu^-}$  for a pair of oppositely-charged muons inside a muon-jet. We show the choice of parameters for case 1 in the Higgs-portal model-2 with  $m_{h_{D_1}} = 2.5$  GeV and  $m_{h_{D_2}} = 0.5$  (left), 1.0 (right). At LHC 14 TeV with Delphes ATLAS simulations.

- 
- [1] M. J. Strassler and K. M. Zurek, Phys. Lett. B **651**, 374 (2007) doi:10.1016/j.physletb.2007.06.055 [hep-ph/0604261].  
T. Han, Z. Si, K. M. Zurek and M. J. Strassler, JHEP **0807**, 008 (2008) doi:10.1088/1126-6708/2008/07/008 [arXiv:0712.2041 [hep-ph]].  
S. Gopalakrishna, S. Jung and J. D. Wells, Phys. Rev. D **78**, 055002 (2008) doi:10.1103/PhysRevD.78.055002 [arXiv:0801.3456 [hep-ph]].  
N. Arkani-Hamed, D. P. Finkbeiner, T. R. Slatyer and N. Weiner, Phys. Rev. D **79**, 015014 (2009) [arXiv:0810.0713 [hep-ph]].  
N. Arkani-Hamed and N. Weiner, JHEP **0812**, 104 (2008) doi:10.1088/1126-6708/2008/12/104 [arXiv:0810.0714 [hep-ph]].  
M. Baumgart, C. Cheung, J. T. Ruderman, L. -T. Wang and I. Yavin, JHEP **0904**, 014 (2009) [arXiv:0901.0283 [hep-ph]].  
M. Reece and L. T. Wang, JHEP **0907**, 051 (2009) doi:10.1088/1126-6708/2009/07/051 [arXiv:0904.1743 [hep-ph]].  
C. Cheung, J. T. Ruderman, L. T. Wang and I. Yavin, JHEP **1004**, 116 (2010) doi:10.1007/JHEP04(2010)116 [arXiv:0909.0290 [hep-ph]].  
A. Falkowski, J. T. Ruderman, T. Volansky and J. Zupan, JHEP **1005**, 077 (2010) [arXiv:1002.2952 [hep-ph]].  
A. Falkowski, J. T. Ruderman, T. Volansky and J. Zupan, Phys. Rev. Lett. **105**, 241801 (2010) doi:10.1103/PhysRevLett.105.241801 [arXiv:1007.3496 [hep-ph]].  
S. Andreas and A. Ringwald, arXiv:1008.4519 [hep-ph].  
Y. F. Chan, M. Low, D. E. Morrissey and A. P. Spray, JHEP **1205**, 155 (2012) doi:10.1007/JHEP05(2012)155 [arXiv:1112.2705 [hep-ph]].
- [2] S. Weinberg, Phys. Rev. Lett. **110**, no. 24, 241301 (2013) [arXiv:1305.1971 [astro-ph.CO]]; K. Cheung, W. Y. Keung and T. C. Yuan, Phys. Rev. D **89**, 015007 (2014) [arXiv:1308.4235 [hep-ph]]; C. F. Chang, E. Ma and T. C. Yuan, JHEP **1403**, 054 (2014) [arXiv:1308.6071 [hep-ph], arXiv:1308.6071].
- [3] R. Dermisek and J. F. Gunion, Phys. Rev. D **81**, 075003 (2010) doi:10.1103/PhysRevD.81.075003 [arXiv:1002.1971 [hep-ph]].  
A. Belyaev, J. Pivarski, A. Safonov, S. Senkin and A. Tatarinov, Phys. Rev. D **81**, 075021 (2010) doi:10.1103/PhysRevD.81.075021 [arXiv:1002.1956 [hep-ph]].  
S. Andreas, O. Lebedev, S. Ramos-Sanchez and A. Ringwald, JHEP **1008**, 003 (2010) doi:10.1007/JHEP08(2010)003 [arXiv:1005.3978 [hep-ph]].
- [4] G. Aad *et al.* [ATLAS Collaboration], Phys. Lett. B **719**, 299 (2013) doi:10.1016/j.physletb.2013.01.034 [arXiv:1212.5409].  
G. Aad *et al.* [ATLAS Collaboration], JHEP **1411**, 088 (2014) doi:10.1007/JHEP11(2014)088 [arXiv:1409.0746 [hep-ex]].  
G. Aad *et al.* [ATLAS Collaboration], arXiv:1511.05542 [hep-ex].
- [5] S. Chatrchyan *et al.* [CMS Collaboration], JHEP **1107**, 098 (2011) doi:10.1007/JHEP07(2011)098 [arXiv:1106.2375 [hep-ex]].  
S. Chatrchyan *et al.* [CMS Collaboration], Phys. Lett. B **726**, 564 (2013) doi:10.1016/j.physletb.2013.09.009 [arXiv:1210.7619 [hep-ex]].  
V. Khachatryan *et al.* [CMS Collaboration], Phys. Rev. D **91**, no. 5, 052012 (2015) doi:10.1103/PhysRevD.91.052012 [arXiv:1411.6977 [hep-ex]].  
V. Khachatryan *et al.* [CMS Collaboration], Phys. Lett. B **752**, 146 (2016) doi:10.1016/j.physletb.2015.10.067 [arXiv:1506.00424 [hep-ex]].
- [6] J. F. Gunion, H. E. Haber, G. L. Kane and S. Dawson, Front. Phys. **80**, 1 (2000).
- [7] J. Chang, K. Cheung and C. T. Lu, Phys. Rev. D **93**, no. 7, 075013 (2016) doi:10.1103/PhysRevD.93.075013 [arXiv:1512.06671 [hep-ph]].
- [8] J. F. Donoghue, J. Gasser and H. Leutwyler, Nucl. Phys. B **343**, 341 (1990). doi:10.1016/0550-3213(90)90474-R
- [9] F. Bezrukov and D. Gorbunov, JHEP **1005**, 010 (2010) doi:10.1007/JHEP05(2010)010 [arXiv:0912.0390 [hep-ph]].
- [10] K. Cheung, J. S. Lee and P. Y. Tseng, Phys. Rev. D **90**, 095009 (2014) doi:10.1103/PhysRevD.90.095009 [arXiv:1407.8236 [hep-ph]].
- [11] J. D. Clarke, R. Foot and R. R. Volkas, JHEP **1402**, 123 (2014) [arXiv:1310.8042 [hep-ph]].
- [12] LHCb Collaboration, LHCb-CONF-2015-002; P. del Amo Sanchez *et al.* [BaBar Collaboration], Phys.Rev. D82, 112002 (2010), arXiv:1009.1529 [hep-ex]; R. Aaij *et al.* [LHCb collaboration], JHEP **1308**, 117 (2013), arXiv:1306.3663 [hep-ex]; J. Lees *et al.* [BaBar collaboration], Phys.Rev. D87, 031102 (2013), arXiv:1210.0287 [hep-ex]; J. Lees *et al.* [BaBar Collaboration], (2012), arXiv:1210.5669 [hep-ex]; J. Lees *et al.* [BaBar Collaboration], Phys.Rev. D88, 031701 (2013), arXiv:1307.5306 [hep-ex].
- [13] R. Aaij *et al.* [LHCb Collaboration], JHEP **1302**, 105 (2013), arXiv:1209.4284 [hep-ex]; J.-T. Wei *et al.* [Belle Collaboration], Phys.Rev.Lett. **103**, 171801 (2009), arXiv:0904.0770 [hep-ex]; B. Aubert *et al.* [BaBar Collaboration], Phys.Rev.Lett. **102**, 091803 (2009), arXiv:0807.4119 [hep-ex]; K.-F. Chen *et al.* [Belle Collaboration], Phys.Rev.Lett. **99**, 221802 (2007), arXiv:0707.0138 [hep-ex]; H. Hyun *et al.* [Belle Collaboration], Phys.Rev.Lett. **105**, 091801 (2010), arXiv:1005.1450 [hep-ex];
- [14] K. Schmidt-Hoberg, F. Staub and M. W. Winkler, Phys. Lett. B **727**, 506 (2013) doi:10.1016/j.physletb.2013.11.015 [arXiv:1310.6752 [hep-ph]].
- [15] S. Chatrchyan *et al.* [CMS Collaboration], Phys. Lett. B **726**, 564 (2013) [arXiv:1210.7619 [hep-ex]]. V. Khachatryan *et al.* [CMS Collaboration], arXiv:1506.00424 [hep-ex].
- [16] S. Chatrchyan *et al.* [CMS Collaboration], JHEP **1107**, 098 (2011) [arXiv:1106.2375 [hep-ex]].

- [17] G. Aad *et al.* [ATLAS Collaboration], Phys. Rev. D **92**, no. 5, 052002 (2015) doi:10.1103/PhysRevD.92.052002 [arXiv:1505.01609 [hep-ex]].
- [18] Some information can be found at [http://atlas.ch/inner\\_detector1.html](http://atlas.ch/inner_detector1.html) and <http://cms.web.cern.ch/news/silicon-pixels>.
- [19] LHC Higgs Cross Section Working Group, <https://twiki.cern.ch/twiki/bin/view/LHCPhysics/CrossSections>
- [20] G. Aad *et al.* [ATLAS Collaboration], Phys. Lett. B **719**, 299 (2013) [arXiv:1212.5409].
- [21] ATLAS Collaboration, Fig. 6 of G. Aad *et al.* [ATLAS Collaboration], “Muon reconstruction efficiency and momentum resolution of the ATLAS experiment in proton-proton collisions at  $\sqrt{s} = 7$  TeV in 2010,” Eur. Phys. J. C **74**, no. 9, 3034 (2014) [arXiv:1404.4562 [hep-ex]]; G. Aad *et al.* [ATLAS Collaboration], Eur. Phys. J. C **74**, no. 11, 3130 (2014) [arXiv:1407.3935 [hep-ex]].  
We used the CB+ST muon efficiency in our Delphes simulation, and the definition of the CB and ST muon efficiencies were listed in Eur. Phys. J. C **74**, no. 9, 3034 (2014) [arXiv:1404.4562 [hep-ex]].
- [22] CMS Collaboration, soft ID for “CMS Performance Note : Muon ID performance: low- $p_T$  muon efficiencies”, CMS DP-2014/020.
- [23] J. Alwall, M. Herquet, F. Maltoni, O. Mattelaer and T. Stelzer, JHEP **1106**, 128 (2011) [arXiv:1106.0522 [hep-ph]].
- [24] J. Alwall and the CP3 development team, *The MG/ME Pythia-PGS package*; the Madgraph at <http://madgraph.hep.uiuc.edu/>; Pythia at <https://pythia6.hepforge.org/>; and PGS at <http://www.physics.ucdavis.edu/~conway/research/software/pgs/pgs4-general.htm>.
- [25] J. de Favereau *et al.* [DELPHES 3 Collaboration], JHEP **1402**, 057 (2014) [arXiv:1307.6346 [hep-ex]].
- [26] For long-lived particle fast detector simulation, we followed the delphes ticket #406 with the TrackVertexSmearing module implemented by Pavel Demin.  
<https://cp3.irmp.ucl.ac.be/projects/delphes/ticket/406>.
- [27] E. Conte, B. Fuks and G. Serret, Comput. Phys. Commun. **184** (2013) 222 [arXiv:1206.1599 [hep-ph]]; E. Conte, B. Dumont, B. Fuks and C. Wymant, arXiv:1405.3982 [hep-ph].
- [28] C. Cheung, J. T. Ruderman, L. T. Wang and I. Yavin, JHEP **1004**, 116 (2010) doi:10.1007/JHEP04(2010)116 [arXiv:0909.0290 [hep-ph]].
- [29] G. Aad *et al.* [ATLAS Collaboration], JHEP **1411**, 088 (2014) doi:10.1007/JHEP11(2014)088 [arXiv:1409.0746 [hep-ex]].  
There are also some other discussions of the efficiency for the displaced muon reconstruction.  
V. Khachatryan *et al.* [CMS Collaboration], Phys. Rev. D **91**, no. 5, 052012 (2015) doi:10.1103/PhysRevD.91.052012 [arXiv:1411.6977 [hep-ex]]. G. Aad *et al.* [ATLAS Collaboration], Phys. Rev. D **92**, no. 7, 072004 (2015) doi:10.1103/PhysRevD.92.072004 [arXiv:1504.05162 [hep-ex]].